THE SIZE DISTRIBUTION OF TRANS-NEPTUNIAN BODIES[1]

G. M. BERNSTEIN AND D. E. TRILLING

Department of Physics and Astronomy, University of Pennsylvania, David Rittenhouse Laboratory, 209 South 33rd Street,
Philadelphia, PA 19104; garyb@physics.upenn.edu, trilling@astro.upenn.edu

R. L. ALLEN

Department of Physics and Astronomy, University of British Columbia, 6224 Agricultural Road, Vancouver, BC V6T 1Z1, Canada;
lallen@astro.ubc.ca

M. E. BROWN

Division of Geological and Planetary Sciences, Mail Code 150-21, California Institute of Technology, Pasadena, CA 91125;
mbrown@gps.caltech.edu

M. HOLMAN

Harvard-Smithsonian Center for Astrophysics, Mail Stop 51, 60 Garden Street, Cambridge, MA 02138;
mholman@cfa.harvard.edu

AND

R. MALHOTRA

Department of Planetary Sciences, University of Arizona, 1629 East University Boulevard,
Tucson, AZ 85721; renu@lpl.arizona.edu

ABSTRACT

We search 0.02 deg^2 of the invariable plane for trans-Neptunian objects (TNOs) 25 AU or more distant using the Advanced Camera for Surveys (ACS) aboard the *Hubble Space Telescope*. With 22 ks per pointing, the search is more than 50% complete for $m_{606W} \leq 29.2$. Three new objects are discovered, the faintest with mean magnitude $m = 28.3$ (diameter ≈ 25 km), which is 3 mag fainter than any previously well-measured solar system body. Each new discovery is verified with a follow-up 18 ks observation with the ACS, and the detection efficiency is verified with implanted objects. The three detections are a factor of ~ 25 less than would be expected under extrapolation of the power-law differential sky density for brighter objects, $\Sigma(m) \equiv dN/dm\, d\Omega \propto 10^{\alpha m}$ with $\alpha \approx 0.63$. Analysis of the ACS data and recent TNO surveys from the literature reveals departures from this power law at both the bright and faint ends. Division of the TNO sample by distance and inclination into "classical Kuiper belt" (CKB) and "Excited" samples reveals that $\Sigma(m)$ differs for the two populations at 96% confidence, and both samples show departures from power-law behavior. A double power-law $\Sigma(m)$ adequately fits all data. Implications of these departures include the following: (1) The total mass of the "classical" Kuiper belt is $\approx 0.010\, M_\oplus$, only a few times Pluto's mass, and is predominantly in the form of ~ 100 km bodies (barring a secondary peak in the mass distribution at sub–10 km sizes). The mass of Excited objects is perhaps a few times larger. (2) The Excited class has a shallower bright-end magnitude (and, presumably, size) distribution; the largest objects, including Pluto, make up tens of percent of the total mass whereas the largest CKB objects are only $\sim 2\%$ of its mass. (3) The derived size distributions predict that the largest Excited body should be roughly the mass of Pluto, and the largest CKB body should have $m_R \approx 20$—hence, Pluto is feasibly considered to have originated from the same physical process as the Excited TNOs. (4) The observed deficit of small TNOs occurs in the size regime where present-day collisions are expected to be disruptive, suggesting extensive depletion by collisions. The Excited and CKB size distributions are qualitatively similar to some numerical models of growth and erosion, with both accretion and erosion appearing to have proceeded to more advanced stages in the Excited class than in the CKB. (5) The lack of detections of distant TNOs implies that if a mass of TNOs comparable to the CKB is present near the invariable plane beyond 50 AU, that distant population must be composed primarily of bodies smaller than ≈ 40 km. (6) There are too few small CKB objects for this population to be the reservoir of Jupiter-family comet precursors without a significant upturn in the population at diameters under 20 km. With optimistic model parameters and extrapolations, the Excited population could be the source reservoir. Implications of these discoveries for the formation and evolution of the outer solar system are discussed.

Key words: Kuiper belt — solar system: formation

1. MOTIVATION

The nebular hypothesis for the formation of planetary systems is nearly 250 years old (Kant 1755), and yet observational support for the model is relatively recent. In the standard scenario, solids in the disk surrounding the protostar begin to coagulate into macroscopic objects, which accrete to kilometer sizes. When the planetesimals become massive enough for gravitational focusing, runaway accretion begins. In the oligarchic growth phase, accretion is limited by excitations in the population induced by the largest few objects. In a protoplanetary disk, these largest planetesimals can reach a

few Earth masses, sufficient to trap the nebular gas, and rapid growth of gas giants can ensue. The nebular gas is cleared by the stellar wind, and the remaining planetesimals are scattered away by the giant planets.

Today we have many observations of dust and gas disks around young stars (O'Dell & Beckwith 1997; Beckwith et al. 2000), evidence that supports the nebular hypothesis. In addition, observations of dust disks around somewhat older stars suggest the presence of a population of dust-producing planetesimals in those systems (e.g., Smith & Terrile 1984; Greaves et al. 1998; Koerner et al. 2001). Some of these dust disks exhibit structures that can perhaps be ascribed to embedded planetary systems (Kuchner & Holman 2003). There is also now abundant evidence for the final stage of accretion—planet formation—as extrasolar giant planets have been detected by radial velocity and transit observations (Marcy et al. 2000). Though the basic idea of the nebular hypothesis remains intact, each new round of observations has led to fundamental changes in our view of planet formation. The presence of gas giants at less than 1 AU, for example, was not well anticipated by theory, and migration is now recognized as an important process.

It is unfortunate that direct observation of planetesimals smaller than 1000 km in extrasolar systems is currently infeasible and likely to remain so for many decades. Such observations would likely reveal further failures of imagination in our modeling of the planetesimal phase. Fortunately, a portion of the Sun's planetesimal population is preserved for our examination in the region beyond Neptune, where growth timescales are longer, the accretion process apparently did not proceed to formation of planets, and the influence of the giant planets was not sufficient to remove all small bodies. Study of trans-Neptunian objects (TNOs) provides "ground truth" for models of the accretion, collisional erosion, and dynamical evolution of planetesimal populations. True to form, the TNO population only vaguely resembles the preconception of a dynamically pristine planetesimal disk. With over 800 TNOs discovered between 1992 and the present, it is clear that the TNO population has several distinct dynamical components, all of which appear to have eccentricity and inclination distributions that are too broad to be the undisturbed remnants of the primordial population. The TNO population contains unmistakable signatures of interactions with Neptune and perhaps other massive bodies. With further study, we can hope to understand the dynamical history of this region.

The physical properties of the TNOs, particularly the size distribution, are indicative of the accretion process. Observations to date are consistent with a distribution of diameters D that is a power law, $dN/dD \propto D^q$ with $q = 4.0 \pm 0.5$ (Trujillo et al. 2001). This distribution must fail at some $D > 0$ to avoid a divergence in the mass or reflected surface brightness of the trans-Neptunian cloud, but the scale of the breakdown in the power law is not usefully bounded by these constraints (Kenyon & Windhorst 2001). In the current dynamical environment, TNO collisions are erosive for objects with diameters $\lesssim 100$ km, so that small objects have been removed from the population since the events or processes that excited the TNO dynamics (Stern 1996). Rather soon after the discovery of the Kuiper belt, there was speculation that the size distribution might break at ∼50 km sizes (Weissman & Levison 1997), but observations to date have not evidenced this phenomenon. A generic prediction of accretion/erosion models is a break to a shallower size distribution below some size, but the size break is dependent upon factors such as the duration of the accretion epoch (Farinella et al. 2000). The mass in the trans-Neptunian region must have been substantially larger in the past in order to support the migration of Neptune (Hahn & Malhotra 1999) and accretion of the present TNO population (Stern 1996), but the relative importance of scattering and collisional grinding in mass removal is unknown.

Extending our knowledge to the faintest (and hence smallest) possible TNOs is clearly desirable, as there may be signatures of the collisional evolution or processes unanticipated by present theory. It is of further interest to see if the size distribution has a dependence upon dynamical properties, as this can provide further insight into the dependence of the accretion/collision process upon the dynamics of the parent population.

The *Hubble Space Telescope* (*HST*) is currently the observatory of choice for detection of the faintest possible point sources. A detection of a very high density of $m_V > 27.8$ TNOs using the Wide Field Planetary Camera 2 (WFPC2) on *HST* is reported by Cochran et al. (1995, hereafter CLSD). For various reasons, it is likely that these detections were merely noise (Brown et al. 1997; Gladman et al. 1998; see Bernstein et al. 2004a for further analysis of the WFPC2 results). The installation of the Advanced Camera for Surveys (ACS) on *HST* subtanstially improved the field of view, efficiency, and sampling. This paper describes the results of a large investment of *HST* time (125 orbits) into a search for TNOs using the ACS.

Detection of faint objects requires long integration times, but a typical TNO moves the width of the *HST* point-spread function (PSF) in only a few minutes. The ACS survey therefore uses a technique we call "digital tracking," in which a long series of exposures is acquired, with each individual exposure short enough to avoid trailing losses. The short exposures are shifted to follow a candidate TNO orbit and then summed, yielding an image with long exposure time that will detect TNOs on the chosen orbit with no trailing. The summation must be repeated for all plausible TNO orbits that diverge by more than the PSF over the time span of the observations. This computationally intensive technique has been used successfully for several ground-based faint-TNO searches (Tyson et al. 1992; Allen et al. 2001; Gladman et al. 1998; Chiang & Brown 1999), and a variant was used by CLSD with WFPC2 data. We are able to detect TNOs to the fundamental limits set by photon noise in the 22 ks total exposure time of each ACS search field. The survey is over 50% complete for $m_{606W} < 29.2$ mag, which is 2 mag fainter than any successful published TNO survey and 1.5 mag deeper than the onset of false positives in the CLSD data. The area covered by the search is 0.02 deg^2, 13 times the area of the CLSD search. The lessons learned from the ground-based and CLSD digital-tracking surveys have helped us to produce results that we believe are optimal and reliable.

The concepts and fundamental limits of digital tracking in this and other applications are detailed in Bernstein et al. (2004a). This paper summarizes the methodology of the ACS search, presents the detections and efficiencies, derives bounds on the apparent magnitude distribution of the TNOs and some dynamical subsamples, and discusses the implications for the evolution of the TNO system. Trilling & Bernstein (2004) present the variability data for the objects detected in the ACS survey. Bernstein et al. (2004b) examines the current state of the art in astrometry for moving objects and the utility of high-precision astrometry for orbit determination.

2. DETECTION TECHNIQUES

The search for moving objects to the photon-noise limit of a 22,000 s ACS integration requires a sophisticated analysis, attention to detail, approximately 30,000 lines of code, and several CPU-years' worth of computation on 2.4 GHz Pentium processors. The unique tools of this data reduction are described in detail in Bernstein et al. (2004a), but we summarize here the aspects that are important for understanding the results.

2.1. *Observations*

The survey covers six slightly overlapping fields of view of the ACS. The spacecraft is oriented so that detector rows and columns are aligned to the local ecliptic cardinal directions. The six pointings are arranged in a 2×3 mosaic, with the long axis in the ecliptic north-south direction. The southern two pointings are labeled A and B, the central two C and D, and the northern two E and F. The ACS pixel scale is nominally $0\rlap{.}{''}050$, and nominal coverage of the full mosaic field of view (FOV) is $\approx 400'' \times 600'' = 0.019$ deg^2. The exposures at a given pointing are dithered by noninteger pixel steps, up to a few pixels, in order to improve the sampling of the static sky objects. The imaged field is not contiguous, because our dithers do not span the gap between the two ACS CCDs.

The field location was chosen subject to a number of criteria. The field center, $14^{\rm h}07^{\rm m}53\rlap{.}{^{\rm s}}3$, $-11°21'38''$ (J2000), is only $3'$ from the invariable plane. The field trails Neptune by $99°$, within the libration region for perihelia of TNOs in 2:1 and 3:2 resonance with Neptune (Malhotra 1996; Chiang & Jordan 2002). A known TNO, 2000 FV$_{53}$, is within pointing A for the full observing period, allowing us to verify our navigation and orbital calculations. The field is placed and the observations timed to minimize the loss of observing time to moonlight and South Atlantic Anomaly crossings, and to place the field $88°$ from opposition at the start of the observing sequence (see below).

All exposures were taken through the F606W filter of the ACS using the Wide Field Channel (WFC). In the period UT 2003 January 26.014–31.341, which we call the "discovery epoch," 55×400 s exposures were taken at each of the six pointings.[2] During 2003 February 5.835–9.703, the "recovery epoch," an additional 40×400 s exposures were taken at each pointing. The two sets of observations, $88°-83°$ and $77°-73°$ from opposition, were chosen to straddle the transition from prograde to retrograde motion for most TNOs. Hence any discovered objects have a maximal chance of remaining in the mosaic FOV for the full 15 day duration of the *HST* observations, and the image trailing due to apparent motion is minimized.

Individual *exposures* are 340–410 s long, averaging 400 s. Five exposures fit into a typical *HST orbit*, with fewer during radiation-impacted orbits. A set of 10 or 15 exposures is taken during each *HST visit* to a given pointing. The pointings are visited in the pattern ABAB-CDCD-EFEF-ABAB-CDCD-EFEF during each of the two *epochs* of observation. So pointing C, for example, is sampled sporadically, at intervals as close as 8 minutes, over a time span of approximately 24 hr, during the first CDCD set of visits. Approximately 2 days later, the CDCD set of visits are repeated. Then, ≈ 7 days later, the cycle repeats for the recovery epoch.

A few shorter exposures of the six pointings and of the outskirts of 47 Tucanae were taken in order to map the WFC

point-spread function and provide astrometric tie-ins. The performance of *HST* and ACS during the observations was nearly flawless. Comparison of the 47 Tuc images before and after the TNO observing cycle showed negligible change in the PSF, so we use a time-invariant (but spatially dependent) PSF map.

2.2. *Preprocessing and "Bright" Object Detection*

Once the data are placed in the *HST* archive, they are prepared for the moving-object search as follows:

1. Bias removal, flat-fielding, and bad-pixel flagging are done by the *HST* "on the fly" processing. Engineering keywords are checked for guiding errors or other problems. The uncertainty images are corrected for some errors in the STScI pipeline, and we create a weight image with the value w at each pixel being $1/\sigma^2$ (where σ is the pixel's flux uncertainty). The weight is zeroed for defective and saturated pixels, and the data and weight images are changed into flux units.

2. Objects in individual exposures are cataloged using SExtractor (Bertin & Arnouts 1996).

3. The exposures of 47 Tuc are used to produce a map of the PSF for the WFC (Bernstein et al. 2004a).

4. WFC distortion maps from STScI or from Anderson (2003) are used to transform pixel positions into a local tangent plane for each exposure, to accuracy ≈ 10 mas; a translation and linear transformation are derived for each exposure to register all the cataloged objects onto a global tangent-plane coordinate system centered on the mosaic center.

5. All exposures from the discovery epoch are combined into a deep image of the fixed sky. This template image has $0\rlap{.}{''}025$ pixels that are square (no distortions) on the global tangent plane, so that the PSF is now sampled near the Nyquist density. Because there are 55 exposures per pointing in the discovery epoch, each template pixel has 10 or more contributing images, and the template noise level is well below the individual exposures'. Sigma-clipping eliminates cosmic rays and bright moving objects from the template images.

6. We interpolate the template image to the location of each pixel of each individual exposure. The interpolated template is then subtracted from each exposure. At pixels with very high flux (centers of bright stars and galaxies), we zero the weight image because the residuals to the template subtraction will rise above the noise. Note that the individual exposures have not been resampled in producing these "subtracted images."

7. Artificial TNOs are added to the subtracted images. One of us (M. H.) produces a list of objects with orbital elements and light-curve parameters selected at random from a chosen range. The positions, magnitudes, and motions of these objects are calculated for each exposure. The position-dependent PSF is trailed for the motion and each artificial object added into the subtracted images, with appropriate Poisson noise in each pixel. One-third of the objects on the list are later revealed to the searchers (G. M. B. and D. E. T.) for use in tuning the search algorithms. The searchers remain blind to the other two-thirds of the artificial objects until after a final TNO candidate list is produced.

8. The subtracted images are searched for potential bright TNOs as follows. A PSF-matched, compensated filter is scanned across each subtracted image. Using the weight image, we can calculate the significance ν (i.e., the signal-to-noise ratio) of each candidate point-source peak in the subtracted image. All peaks with $|\nu| \geq 3.5$ are noted and the χ^2 of a fit to the PSF is calculated. Those that sufficiently resemble the PSF

---

[2] Exposure times varied slightly because of spacecraft constraints.

are recorded to a file of bright-TNO candidates, to be examined later. Note that real TNOs will not fit the PSF precisely, because of trailing, so our criterion for matching the PSF is kept loose, and the vast majority of candidates are cosmic rays.

9. The subtracted images are "cleaned" in preparation for the faint-object search as follows. Every pixel in the subtracted image that deviates by more than 5σ from the mean sky level is flagged. All weights are set to zero within a 2 pixel radius of each flagged pixel. This effectively masks all cosmic rays and non-Gaussian noise in the subtracted images, which is extremely important for avoiding false positive detections in the faint-object search. This process also masks bright TNOs and asteroids; the former have already been detected, however, in the previous step.

10. A "flux image" is now created for each exposure. The flux image is created on a regular grid in the global tangent-plane coordinates. Each such grid point is mapped back to a pixel position on the masked subtracted image, and we record the best-fit PSF flux and its uncertainty for a point source at that location. Hence the "flux image" is a map of the brightness of a potential point source at any location in that exposure, and a weight (uncertainty) image is propagated as well. These flux images are the raw material for the faint-object search.

Any potential bright moving objects must now be found on lists produced in step 8, because the masking in step 9 may preclude their later detection. "Bright" in this context means detectable at $\geq 3.5 \sigma$ in a single 400 s *HST* exposure, which in practice corresponds to $m \leq 27.6$. We use here and henceforth the *HST* F606W magnitude system unless otherwise noted. The filter passband is roughly the union of V and R passbands, and the AB zero point is similar to a V zero point.

Over 900,000 flux peaks trigger the $\nu \geq 3.5$ threshold in the discovery epoch. To fish the real (and implanted) TNOs from this sea of cosmic rays, we first require that a flux peak repeat in the same sky location (to $0\rlap{.}''2$) on successive exposures in one orbit, leaving 7700 pairs of detections. We reject linked detections that occur on the same detector pixels to avoid CCD defects. We next require *two* pairs of detections to exist within the same visit and be within $\approx 2''$ hr^{-1} of each other, leaving 1300 candidate quadruples of detections. Next a preliminary orbit is fitted to each quadruple, and the methods of § 2.3.2 are used to check whether the subtracted images are consistent with a point source moving on the putative orbit. This reduces the candidate list to 49 objects, of which 46 are then revealed to be on the artificial-object list. The detection efficiency of the bright search for artificial objects is found to be 100% for $m \lesssim 27.6$.

The three remaining objects are real: one is 2000 FV$_{53}$, the previously known object, which at $m = 23.4$ is blindingly bright here, appearing at $\nu \approx 80$ in each of the 55 discovery-epoch exposures and 40 recovery-epoch exposures. The second bright detection is a new object, now given the preliminary designation 2003 BG$_{91}$, with time-averaged magnitude $\langle m \rangle = 26.95 \pm 0.02$. The third detection from the bright search, 2003 BF$_{91}$, has $\langle m \rangle = 28.15 \pm 0.04$ but is highly variable and rises above the $\nu = 3.5$ single-exposure threshold several times. The bright-object search is executed independently on the recovery-epoch observations, revealing the same three objects, which are thus undoubtedly real.

2.3. *Faint-Object Search*

The search for moving objects that are below the single-exposure detection threshold is much more computationally intensive. We must sum the available exposures along any potential TNO path through the discovery-epoch exposures and then ask whether the best-fit flux for this path is safely above the expected noise level.

2.3.1. *The Search Space*

The space of TNO orbits is six-dimensional, with one possible parameterization being $\{\alpha, \beta, d, \dot{\alpha}, \dot{\beta}, \dot{d}\}$, where α and β are the angular position relative to the center of the mosaic at some reference time T_0, d is the geocentric distance at T_0, and the overdots denote the TNO's space velocity in the same basis (cf. Bernstein & Khushalani 2000). The line-of-sight motion $\dot{d}$ has negligible observable effect over the course of the 15 day *HST* observation, so we may set it to zero in our searches. This means we have five dimensions of TNO orbit space to search. We search on a grid of points in this space. The grid spacing in α and β is the pixel scale P of the flux images discussed above. The grid spacing Δv in the velocity space $(\dot{\alpha}, \dot{\beta})$ should be fine enough that tracking errors are held to less than 1 pixel: $\Delta v \leq P / \Delta T$, where ΔT is the time span of the observations being combined. Finally we must choose a grid in distance d. The primary effect of d upon the apparent motion of the TNO is from the reflex of Earth's orbit around the Sun (and *HST*'s orbit around Earth). The reflex motions scale as $1/d$, so we choose a grid that is uniform in $\gamma \equiv 1/d$. We also note that the nonlinear components of the TNO apparent motion all depend solely upon γ—primarily the reflex of Earth's orbital acceleration, but also the Newtonian gravitational acceleration of the TNO itself. The spacing $\Delta \gamma$ must be fine enough that errors in these nonlinear motion components are held to $\ll P$.

The number of grid points that must be searched then scales roughly as $P^{-5} \Delta T^3$. We conduct our faint-object search in two passes: first with $P = 0\rlap{.}''050$, and then a finer pass with $P = 0\rlap{.}''030$. The first pass runs quickly enough to have been completed between receipt of the *HST* data in mid-February and scheduled follow-up observations at the Keck and Magellan telescopes in late April (see § 2.4). But the PSF of the WFC is only $0\rlap{.}''05$ across, so mistracking by $\approx 0.5P$ at $P = 0\rlap{.}''05$ causes significant blurring of the PSF in digitally tracked images, degrading our magnitude limit by ≈ 0.2 mag. Hence we later run the finer grid search to reach the ultimate limit of the WFC data.

The bounds of the search space are determined as follows:

a) We search $25 \text{ AU} < d < \infty$. Even objects at $d \approx 1000$ AU would move several ACS pixels over the course of our visits.

b) The perihelion of the orbit is constrained to be ≥ 10 AU. This places a lower limit on the transverse motion at a given d.

c) The orbit is assumed to be bound. This places an upper limit on the transverse motion at a given d.

d) The inclination of the orbit is assumed to be $i < 45°$. This bounds the vertical component of the apparent motion. Note that we search only prograde orbits.

2.3.2. *Steps for the Faint Search*

The faint search proceeds after step 10 above as follows for each of the coarse $P = 0\rlap{.}''05$ (discovery and recovery epochs) and the fine $P = 0\rlap{.}''03$ (discovery only) searches:

1. The flux images produced for this P in the search are split into six *sets* of visits. Set 1 contains the first ABAB sequence, set 2 the first CDCD sequence, etc. The digital-tracking sums will be accumulated over a set's worth of

images, with time span $\Delta T \lesssim 24$ hr. Digital tracking over the full 5 day time span of the discovery epoch would be computationally infeasible.

2. For each set, the outermost loop is over the distance grid. The next inner loop is over the velocities $\dot{\alpha}$ and $\dot{\beta}$. At a given distance and velocity, we calculate an orbital shift for each exposure relative to the first exposure. The inner loops consist of summing the individual flux images at each pixel, with integer pixel shifts defined by the velocity and distance.

In the fine search, there are 13 distance grid points and a total of $\approx 7 \times 10^5$ velocity grid points in the $\{\dot{\alpha}, \dot{\beta}, d\}$-space. For each set there are two pointings spanning $\approx 1 \times 10^8$ pixels in the flux images, with 25–30 exposures per pixel per set. In total, the fine search tests $\approx 10^{14}$ points in the TNO phase space, requiring $\approx 10^{16}$ pixel additions to do so. This takes several CPU-years for 2.4 GHz Pentium 4 processors, but a cluster of 10 CPUs at Penn and eight at Arizona reduces the required real time.

3. At each grid point of the TNO search, the point-source fluxes along the track of the putative TNO from all exposures in the set are summed, as weighted by their inverse uncertainties, to form a total best-fit flux and uncertainty. If the significance $\nu \equiv f/\sigma_f$ exceeds a threshold of 4.0, the grid point is saved.

4. Above-threshold grid points that abut in phase space are aggregated, and the most significant is saved. The output of the fine search is a list of $\approx 1.5 \times 10^8$ significance peaks in the TNO phase space.

5. For each detected peak a "tune-up" program is run, which fits a model moving point source to the pixel values in postage stamps from all subtracted images. The gridded peak is the starting point, and α, β, $\dot{\alpha}$, and $\dot{\beta}$ are allowed to vary. The significance of real (or implanted) objects typically rises after tune-up, since the optimized orbit is a better fit than the nearest grid point, and the position and velocity estimates become more accurate. Significance peaks that are noise tend, however, to become less significant, to have poor χ^2, and/or to fail to converge. The tune-up step reduces the number of $\nu \geq 4.0$ peaks in the fine search to 6×10^7.

6. The tuned-up peak catalog from one set is now compared with all other sets of the epoch; any pair of peaks that might correspond to a common orbit are linked and passed to the next step. Note that TNOs that cross the boundaries of the ACS pointings are found as efficiently as those that do not. There are 3×10^5 (nonunique) linked peak pairs in the fine search, of which 3×10^4 have total significance $\nu \geq 7$.

7. All the linked pairs with $\nu \geq 7$ are again run through the tune-up program, but this time all of the exposures from the entire epoch are used. The arc is now sufficiently long (typically 3 days) that we can allow the distance d to vary without fear of degeneracy. A few detection candidates with $\chi^2 - \mathrm{dof} > 150$ in the fit of the moving-source model to the data are rejected; inspection shows these to be spurious detections near the residuals of diffraction spikes of bright stars. We apply a threshold of $\nu \geq 8.2$ ($\nu \geq 10$ for the coarse search) to obtain the TNO candidate list of ≈ 100 objects.

The histogram of detections versus significance rises very rapidly below $\nu = 8.2$, which is to be expected from Gaussian noise in a search of 10^{14} or so phase-space locations (Bernstein et al. 2004a). The threshold is placed at the tail of this false-positive distribution. Detection candidates above this threshold are inspected by eye, with two to three being clearly associated with subtraction residuals and other data flaws.

In the coarse search, there were 92 detections with $\nu \geq 10$. The blind list of artificial TNOs was then revealed, and 89 of the 92 were found to be implanted objects. Two of the remaining detections, 2000 FV_{53} and 2003 BF_{91}, coincide with bright detections. The last is a new object, 2003 BH_{91}, discovered with significance $\nu = 16.7$ and mean magnitude $m = 28.35$.

For the fine search (which had an independent set of implanted objects), there were 67 detections, of which 64 were found to be on the list of implanted TNOs. The three remaining detections are again 2000 FV_{53}, 2003 BF_{91}, and 2003 BH_{91}.

The faint-search technique was also applied to the recovery epoch with a coarse ($P = 0\rlap{.}''05$) grid. The same candidates were independently detected above the $\nu = 10$ threshold. Figure 1 shows postage-stamp images of 2000 FV_{53} and the three new detections, as we improve the depth of images by summing more exposures.

2.4. Orbit Determination and Recovery

Each of the TNOs detected in the discovery epoch is also clearly detected in the recovery epoch. We now combine the information from all exposures in the entire ACS campaign to get the best possible constraint on each object's orbit. We again invoke the tune-up program, whereby the orbital parameters are varied to maximize the significance of the detection of the moving point source. More specifically, the orbital parameters determine the location of the PSF and the degree of trailing in each individual exposure. The two endpoints of the trail are converted into pixel coordinates using the registration information and the distortion maps. We calculate the PSF at the TNO location using the spatially varying PSF maps from 47 Tuc, and we smear this PSF to the required trail length. The flux of the TNO is allowed to vary in a stepwise fashion from orbit to orbit (or from exposure to exposure for the high signal-to-noise ratio 2000 FV_{53}). A model with constant flux for a given TNO would be a poor fit, as all the detected objects have significant flux variations. The moving, variable-flux model is then fitted to the subtracted images, with all orbital elements and fluxes being optimized. A by-product of this orbital optimization is an optimally measured light curve for each object. Analysis and interpretation of these light curves is presented in Trilling & Bernstein (2004).

For the final orbit determination, all six orbital parameters are allowed to vary. The 2000 FV_{53} data are of such high quality—positional accuracy of ~ 1 mas for each of the 95 exposures—that the line-of-sight velocity, and hence a and e, are significantly constrained with only a 13 day arc. Bernstein et al. (2004b) will consider in detail the techniques, limitations, and benefits of such high-precision astrometry for the determination of solar system orbits.

For the three newly detected objects, the line-of-sight motion is still poorly determined over the 13 day arc. In the final orbit fit to the *HST* data, we include a prior constraint on the kinetic and potential energies that weakly pushes the orbit to circularity:

$$\chi^2_{\mathrm{prior}} = 4(2\,\mathrm{KE}/\mathrm{PE} + 1)^2. \qquad (1)$$

An unbound or plunging orbit is thus penalized as a 2 σ deviation. The results of the fitting process are best-fitting orbital parameters (in the $\{\alpha, \beta, \ldots\}$ basis) for each object *and* covariance matrices for each, which can be used as described
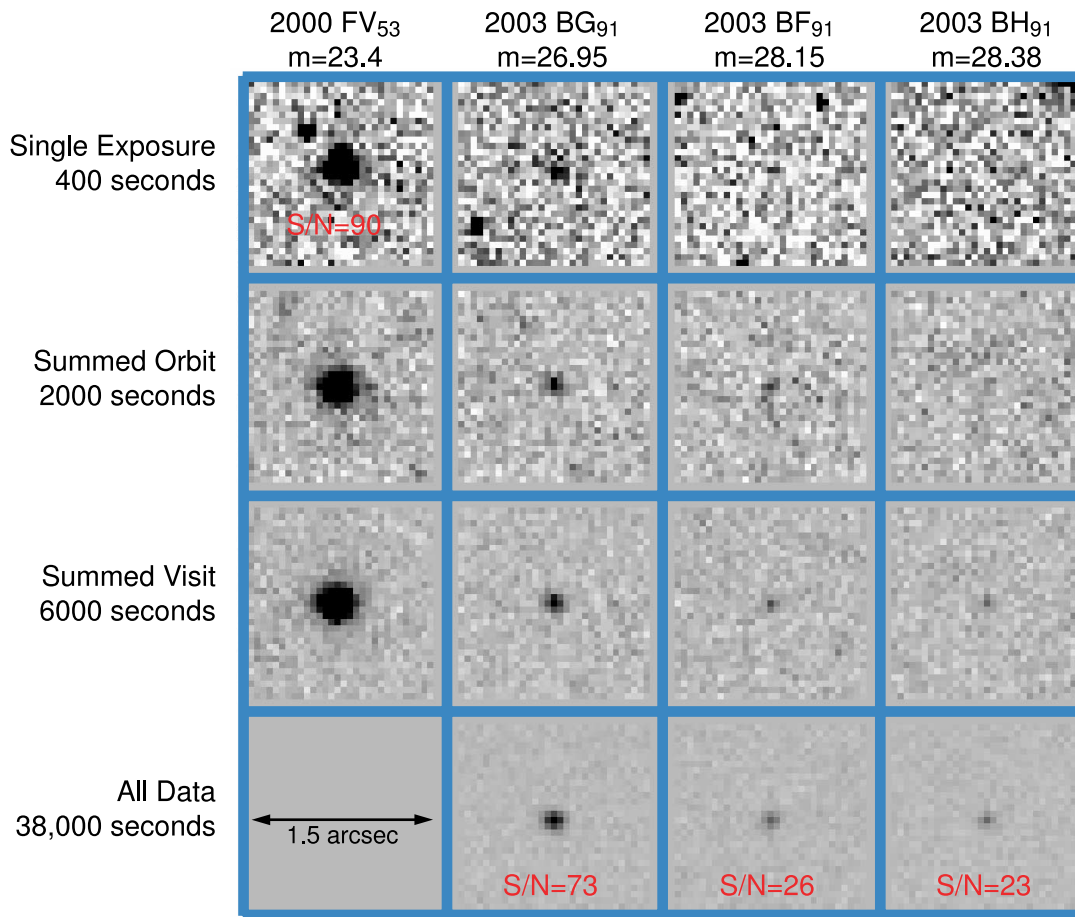
Fig. 1.—Postage-stamp digitally tracked images of all four TNOs detected in the ACS data. Successive rows show images with more contributing integration time, starting with a randomly selected single exposure and ending with the summed image of all available ACS data. All images are shown with the same gray scale. The bottom row gives the final signal-to-noise ratio of each object, save 2000 FV$_{53}$, for which the full-survey sum is omitted and the S/N per exposure is listed. Note that the faintest object is undetectable on single exposures and yet is 0.8 mag brighter than our estimated completeness limit.

in Bernstein & Khushalani (2000) to give orbital elements and position pre-/postdictions with associated uncertainties.

We attempted retrieval of all new objects using the imaging mode of the DEIMOS instrument on the Keck II Telescope on the nights of 2003 April 27 and 28. The error ellipses for all three objects fit within a single DEIMOS field of view, so for each object we have 5 hours of integration in the R band on each of two nights. We sum the Keck exposures to follow the motion vectors predicted for the TNOs by the *HST* data. Object 2003 BG$_{91}$ is detected at $R \approx 27$ on each night, but 2003 BF$_{91}$ and 2003 BH$_{91}$ remain below the detection threshold. Attempts to retrieve the objects with the

Magellan II telescope on 2003 June 1–2 were foiled by poor weather.

The orbital constraints are now refined using the Keck position. Table 1 gives the discovery circumstances and best-fit orbital elements for each object. They all have orbits consistent with "classical Kuiper belt" (CKB) objects, with distances of 40–43 AU and inclinations of $\leq 3°$. The orbital eccentricities either are (2003 BG$_{91}$) or are consistent with (2003 BF$_{91}$, 2003 BH$_{91}$) $e < 0.08$. It is interesting to note that no Plutinos were discovered despite the fact that our observations were in the longitude region where Plutinos reach perihelion. Likewise, no high-eccentricity or distant objects

TABLE 1

PROPERTIES AND BARYCENTRIC ELEMENTS OF DETECTED OBJECTS

Name	d^{a} (AU)	a (AU)	e	i (deg)	Mean F606W Magnitude	Diameter[b] (km)
2000 FV$_{53}$[c]............	32.92 ± 0.00	39.02 ± 0.02	0.156 ± 0.001	17.35 ± 0.00	23.41 ± 0.01	166
2003 BG$_{91}$............	40.26 ± 0.00	43.29 ± 0.06	0.071 ± 0.004	2.46 ± 0.00	26.95 ± 0.02	44
2003 BF$_{91}$	42.14 ± 0.01	50 ± 20	0.4 ± 0.4	1.49 ± 0.01	28.15 ± 0.04	28
2003 BH$_{91}$............	42.55 ± 0.02	45 ± 13	0.2 ± 0.7	1.97 ± 0.02	28.38 ± 0.05	25

[a] Heliocentric distance at discovery.
[b] Assuming a spherical body with geometric albedo of 0.04.
[c] Previously known TNO targeted for this study. Elements reported here are from ACS data alone.

were found. The implications of their absence are discussed below.

2.5. Detection Efficiencies

We next address the important issue of whether our TNO search is complete (i.e., free of false negatives) and reliable (free of false positives).

2.5.1. Reliability

We are claiming to have examined over 10^{14} possible TNO sites in phase space and have exactly zero false positives with $\nu > 8.2$. This is not a trivial issue, as more than one publication claiming detection of TNOs at $R > 26$ has upon further examination been found (Brown et al. 1997; Gladman et al. 2001) to have primarily false positive detections. In the ACS program, however, the detections are unambiguous: each of the three new objects is independently detected in the recovery epoch as well as the discovery epoch. Furthermore, the one sufficiently bright object is recovered at Keck.

2.5.2. Completeness

Is the search complete? This issue is addressed primarily through the implantation and blind retrieval of artificial TNOs. We implant two distinct sets of artificial TNOs into the discovery-epoch data: one for the coarse search and one for the faint search. In each case, the artificial TNO orbital elements are chosen at random from a constrained range of the element space. The range of elements is carefully chosen so that the artificial objects overfill the ranges of position, velocity, distance, and magnitude to which the search is sensitive.[3] From the randomly selected elements, we can then calculate the geometric search area by noting which objects fall into the field of view for the requisite number of exposures. From the final object list in each search, we calculate the probability of detection for objects that meet the geometric criteria. The product of these two is the *effective area* Ω_{eff}, which will be a function of apparent magnitude and could depend upon such quantities as distance, rate of motion, and light-curve amplitude.

For the coarse search, ≈ 150 implanted TNOs have $27.3 < m < 29.4$ and light-curve amplitudes up to 0.2 mag. In the bright search, 46 of these are recovered, and 89 are recovered in the faint/coarse search. From these we verify that there is no gap between the magnitude ranges for which the bright search and the faint search are 100% effective. The area lost to bright stars and galaxies is negligible because the PSF of ACS images is very small, and is also stable, so the fixed-sky subtraction is very successful. The effective area has no detected dependence upon TNO distance or velocity within our TNO phase space search grid. This is expected, since all TNOs should move several pixels from orbit to orbit yet have average trailing loss of less than 0.1 mag.

For the faint search, artificial TNOs are generated with $28.6 < m < 29.4$ in order to more carefully probe the limiting magnitude of the survey. A TNO is considered to be in the survey area if it is imaged in at least three of the *HST* visits of the discovery epoch; 101 artificial TNOs meet this criterion, of which 64 are detected at $\nu \geq 8.2$. Figure 2 plots the recovery efficiency versus mean magnitude for the faint
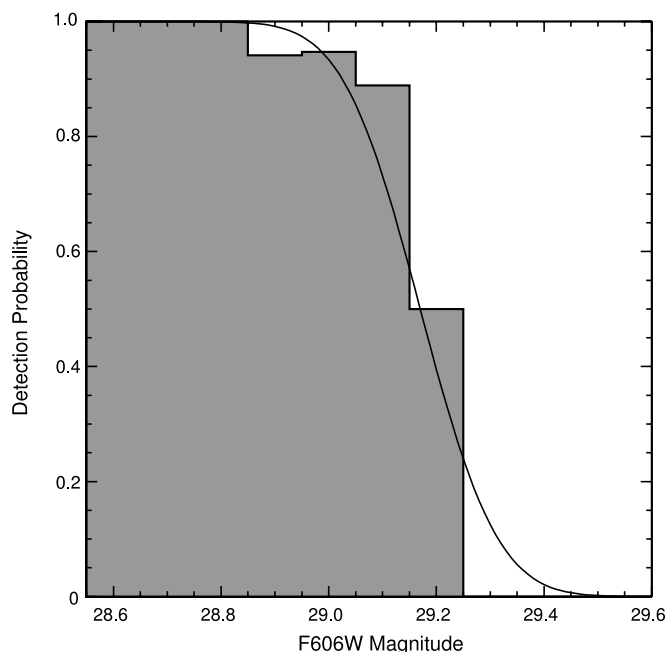

Fig. 2.—Probability of detection vs. mean measured magnitude for the artificial TNOs in the fine search of the discovery epoch. The histogram gives the results from the 101 artificial objects within the FOV, and the curve is eq. (2).

search. The effective area versus magnitude is well described by

$$\Omega_{eff} = (\Omega_0/2) \, erfc \, [(m - m_{50})/2w], \qquad (2)$$

where $\Omega_0 = 0.019 \ deg^2$ is the peak effective solid angle, $m_{50} = 29.17$ is the F606W magnitude at which the effective area drops 50%, and $w = 0.08$ mag is a transition width. The detection efficiency again has no measurable dependence upon distance or velocity over the search space.

Why should we trust the artificial-TNO tests to verify our completeness? After all, if the implantation process and the search/extraction process make common errors in flux scale, orbit calculation, PSF shape, or image distortion, then the artificial objects could be detected at high efficiency while real objects are not.

We note first that the orbit calculation code used for object implantation was written by one of us (M. H.), while that used for extraction was independently written by another (G. M. B.), and both codes were checked against each other and the JPL online Horizons service.[4]

The targeted TNO 2000 FV_{53} helps us to address concerns about errors in orbit calculations, image registration and distortion, and PSF estimation. The individual exposures for 2000 FV_{53} are fitted by our moving-PSF model to good precision: its positions match the extrapolation of previous observations to the accuracy of the extrapolation, and we find the positions consistent with a refined orbit to the level of ≈ 3 mas, or less than 0.1 pixels on the WFC. This is better than the claimed accuracy of the distortion map. We are thus reassured that our models and code for spacecraft navigation, image registration, orbital motion, and field distortion are correct to the accuracy required for the search. The images of 2000 FV_{53}

---

[3] The inclination range of artificial TNOs is limited because of a software bug. We also do not place artificial TNOs at $d \gtrsim 200$ AU.

[4] See http://ssd.jpl.nasa.gov/horizons.html.

are formally inconsistent with the PSF model ($\chi^2/\mathrm{dof} > 1$), but this is because the signal-to-noise ratio of the 2000 FV_{53} observations is very high. The deviations from the fit are at the level of a few percent of the PSF, and hence the PSF model is sufficiently accurate for the fainter detections.

2.5.3. A Caveat on Light Curves

The selection function for TNOs with variable magnitude is complex: the object must be seen during at least three, and preferably four, *HST* visits with a signal-to-noise ratio of $\gtrsim 4$ to survive the detection cuts. The timing of these visits is irregular, and hence there is no simple way to quantify the impact of light-curve variation on detectability. The implanted TNOs were given sinusoidal light curves with peak-to-peak amplitudes chosen uniformly between 0 and 0.2 mag and periods chosen uniformly between 0.05 and 1.3 days—in this range, we did not note any change in detection probability versus magnitude. We know, however, that there exist TNOs with light-curve amplitudes near or above 1 mag, such as 2003 BF_{91} (Trilling & Bernstein 2004) and 2001 QG_{298} (Sheppard & Jewitt 2004), and we should investigate the effects of high variability upon the detection properties of our and other surveys. Subtle biases on light-curve shape are present for all TNO surveys, though other authors have chosen, like us, to ignore them for simplicity. In the Appendix we demonstrate that these biases are too small to be significant with current data but may be important for future larger surveys.

3. CONSTRAINTS ON THE TRANS-NEPTUNIAN POPULATION

The ACS survey detects a total of three objects (not counting the targeted 2000 FV_{53}), described in Table 1, over an effective search area described by equation (2). Trujillo et al. (2001, hereafter TJL) fitted a power law to the cumulative ecliptic surface density distribution of TNOs:

$$N(<R) = 10^{\alpha(R-R_0)} \ \mathrm{deg}^{-2} \qquad (3)$$

with R being the R-band apparent magnitude, $\alpha = 0.63 \pm 0.06$, and $R_0 = 23.0$. Their fit is to survey data over the range $19 < R < 27$. Taking our limit $m_{50} = 29.17$ to be equivalent to a limit of $R \leq 28.8$ (§ 3.1), an extrapolation predicts ≈ 85 detectable objects in our survey. This is quite inconsistent with our observation—even the TJL 2 σ limit of $\alpha = 0.51$ predicts ≈ 16 detections in our survey—and it is immediately obvious that the magnitude (and hence size) distribution of TNOs changes behavior somewhere in the $25 < m < 29$ range. In this section we quantify the nature of this breakdown in the single power law and calculate the implications for integral properties of the TNO population.

3.1. Compendium of TNO Survey Data

We wish to derive the differential surface density $\Sigma(R) \equiv dN/dR\,d\Omega$ of TNOs per R-magnitude interval using all possible reliable published survey data. The requirements for published survey data to be useful are the following:

1. The coordinates of all fields searched must be given.
2. The effective search area as a function of m for each field must be given, preferably derived by Monte Carlo tests.
3. The circumstances of discovery of all detected objects must be given, including apparent magnitude, estimated heliocentric distance d, and estimated inclination i of the orbit.

Note that we do not require that all detected objects have fully determined orbits. While the $R \leq 24$ TNO discoveries have been recovered with admirable completeness, the practical difficulties of recovery for fainter objects have precluded observational arcs longer than ≈ 1 day for any object with $R > 25.6$ (prior to this ACS survey). Fits to 1 day arcs yield d and i to 10%–20% accuracy, but other orbital properties are highly degenerate. Hence, a comprehensive study of both and bright and faint detections can as yet make use only of d and i to categorize the TNOs.

The sky-plane density of TNOs is certainly a function of latitude relative to the midplane of the population. Most of the $R > 22$ searches have been targeted to the ecliptic plane or, less frequently, the invariable plane. Brighter surveys cover a larger area and have ranged farther from the ecliptic. Proper comparison of bright- and faint-TNO densities requires that we consider sky densities measured within a fixed band of TNO latitude. If the latitude distribution of TNOs were well known, we could make use of all the available survey data. While the midplane of the TNO population has recently been estimated to be $\approx 0°.7 \pm 0°.4$ from the invariable plane (Brown & Pan 2004), the full distribution remains poorly constrained. We restrict the published survey data compendium to fields with invariable latitude $\leq 3°$. The TJL estimate of the inclination distribution of bright CKB objects (CKBOs) implies a drop by a factor of ≈ 2 in the sky-plane density from $0°$ to $3°$ *ecliptic* latitude, so there may remain substantial inhomogeneity in comparing surveys over a $\pm 3°$ swath. Attempts to select a narrower latitude range are counterproductive, however, given our poor knowledge of the sky distribution of TNOs.

The resonant TNO population has longitudinal structure in the sky-plane density as well, with more objects being found at bright magnitudes in the directions perpendicular to Neptune. Plutinos (3:2 Neptune resonators) have perihelion positions that librate about these points. This longitude variation has yet to be mapped in any way, so a correction is not possible. The effect upon our results is not likely to be significant, because surveys at all magnitudes span a range of longitudes. The exception is our uniquely deep ACS field, which though pointed in the region of Plutino perihelion libration does not detect any Plutinos. Our most precise analyses will in any case be done on samples intended to exclude Plutinos.

A subtle difference between the bright and faint TNO samples is that the former are typically discovered on single short ($\lesssim 10$ minute) exposures and, hence, measure the *instantaneous* magnitude distribution. Objects with $R > 25$ are detected in summations of many hours' worth of exposures and depend upon the flux of the TNOs *averaged over their light curves* (see also discussion in § 2.5.3). In the Appendix we show that this effect is insignificant for the current data.

We list in Table 2 the published TNO surveys that meet the requirements. We restrict our consideration to those works that dominate the surveyed area at a given magnitude, and we omit surveys that have been shown to contain significant false-positive contamination. For the purposes of the $\Sigma(R)$ analysis, we wish to standardize all magnitudes to the R band. The La and CB data are reported in the V band; Tegler & Romanishin (2003) present accurate colors for many (bright-end) TNOs, and the mean $V-R$ is ≈ 0.6 mag, which we apply to the V detections. Some of the ABM fields use a "VR" filter, so for these we apply the color correction given by Allen et al., assuming again $V-R = 0.6$ for an average TNO. The F606W filter on the ACS WFC is essentially the union of the V and R

TABLE 2
SUMMARY OF TNO SURVEYS

Abbreviation	Reference	Ω_{eff}[a] (deg[2])	m_{50}[a]	N(CKBO)[b]	N(Excited)[b]	$P(\leq N)$[c]	Q_{AD}[c]	$P(\leq \mathcal{L})$[c]
ACS.............	This work	0.019	28.7	3	0	0.16	0.65	0.42
CB	Chiang & Brown 1999	0.009	26.8	1	1	0.98	0.91	0.09
Gl	Gladman et al. 2001	0.322	25.9	8	9	**0.98**	**0.03**	0.83
ABM	Allen et al. 2002	2.30	25.1	17	15	0.49	0.18	0.58
TJL	Trujillo et al. 2001	28.3	23.8	39	28	0.27	0.44	0.27
La	Larsen et al. 2001	296	20.8	1	5	**0.97**	**0.05**	0.30
TB	Trujillo & Brown 2003	1430	20.2[d]	0	2	0.28	0.63	0.58

[a] Effective search area within $3°$ of the invariable plane at bright magnitudes, and R magnitude at which effective area drops by 50%.
[b] Number of detected TNOs in the two dynamical classes defined in the text.
[c] Cumulative probabilities of this survey under the best–fit two–power-law model, for Poisson test, Anderson-Darling test, and $\mathcal{L}$-tests, as described in the text. Boldface marks indications of poor fits.
[d] The TB data are not used faintward of 20.2 mag.

passbands. Tegler & Romanishin show that the average TNO is ≈ 0.39 mag redder in $V-R$ than the Sun, so we presume that the average $m_{606W}-R$ TNO color is about 0.20 mag redder than solar. Taking the solar $V-m_{606W} = 0.06$ mag from the ACS Instrument Handbook, an average TNO should have $m_{606W}-R \approx 0.4$ mag. We correct the ACS limits and detections to R using this value. Henceforth we will use only R-band magnitudes. In the Appendix, we show that variance in $V-R$ colors of TNOs has a negligible effect upon our analysis of the current data.

Some other adjustments to the published survey data are necessary:

1. The effective search area of each Larsen et al. (2001) field is taken to be the product of its geometric area and the $F(T)$ entry denoting the fraction of the field that is estimated to be unique to the survey in their Table 1. We crudely fit a completeness model in the form of equation (2) to the completeness for each seeing bin listed in their Table 3. The effective area of all search fields centered within $\pm 3°$ invariable latitude are summed to give a total useful survey area for the survey, and we only count objects detected in these low-latitude fields. The redundancy and broad latitude coverage of this survey mean that its peak effective area, for our purposes, is only 20% of its raw angular coverage.

2. In the TJL data, no distance or inclination information is available for seven of 74 objects detected near the ecliptic plane. TJL note that this information is missing because of inclement weather at follow-up time and therefore these seven objects should be drawn from the same distribution as the remainder. We therefore omit these seven from our listing and decrease the tabulated effective areas by $7/74 = 9.5\%$ in order to reflect this follow-up inefficiency.

3. Allen et al. (2001) and Allen et al. (2002) are merged for this analysis.

4. Gladman et al. (2001) describe two searches, one with the Canada-France-Hawaii Telescope and one with the VLT. We sum their effective areas and detections in this analysis.

5. Trujillo & Brown (2003) do not give individual field coordinates, but they do give the total sky coverage as a function of invariable latitude, which suffices for our purpose. This preliminary report does not include a detection-efficiency analysis, merely an estimate of a 50% completeness level $R \approx 20.7$. We avoid this uncertainty by making use of the TB data only for $R < 20.2$ and assuming that in this range the detection efficiency is a constant 85% over the surveyed area.

Note that the effective search area of TB comprises the majority of the $\pm 3°$ latitude region.

6. The brightest surveys (Trujillo & Brown 2003; Larsen et al. 2001) have inaccurate magnitudes for their detections, due to varying observing conditions and ill-defined passbands. Nearly all these objects have, however, been carefully reobserved by other authors for color and variability information, and we can replace the original survey magnitudes with highly accurate R-band mean magnitudes. The original magnitude uncertainties remain relevant, however, for treatment of incompleteness, as discussed in the Appendix.

7. We truncate all the efficiency functions η to zero when they drop below $\approx 15\%$ of the peak value for that survey and ignore detections faintward of this point. In this way we avoid making our likelihoods sensitive to rare detections in the (poorly determined) tails of the detection function.

We define three dynamical groupings of the detected TNOs in these surveys:

a) The *TNO* sample holds all objects discovered at heliocentric distances $d > 25$ AU. One known Centaur (1995 SN$_{55}$) sneaks into this TNO sample, but we do not omit it, because similar objects found in the faint sample would not have been rejected.

b) The *CKBO* sample is the subset of the TNO sample having 38 AU $< d <$ 55 AU and $i \leq 5°$. This is intended to exclude resonant and scattered objects to the extent possible with our limited orbital information.

c) The *Excited* sample is the complement of the CKBO sample in the TNO sample. High inclinations and/or proximity to Neptune would indicate substantial past interactions with Neptune or another massive body.

Note that we have used ecliptic inclinations rather than invariable, since the latter are not generally available. We have used the central values for d and i even when the surveys report uncertainty ranges that cross our definitional boundaries. We have ignored the possibilities of overlaps in survey areas and omitted targeted objects such as 2000 FV$_{53}$.

The TNO sample under analysis thus contains 129 detections spanning $19.5 \leq R \leq 28.0$, of which 69 are assigned to the CKBO class. Figure 3 shows the Ω_{eff} of the published surveys versus magnitude, and the binned magnitude distribution of the detections.

Our definition of the CKBO class is imperfect because we are restricted to the use of d and i in classification. Resonant
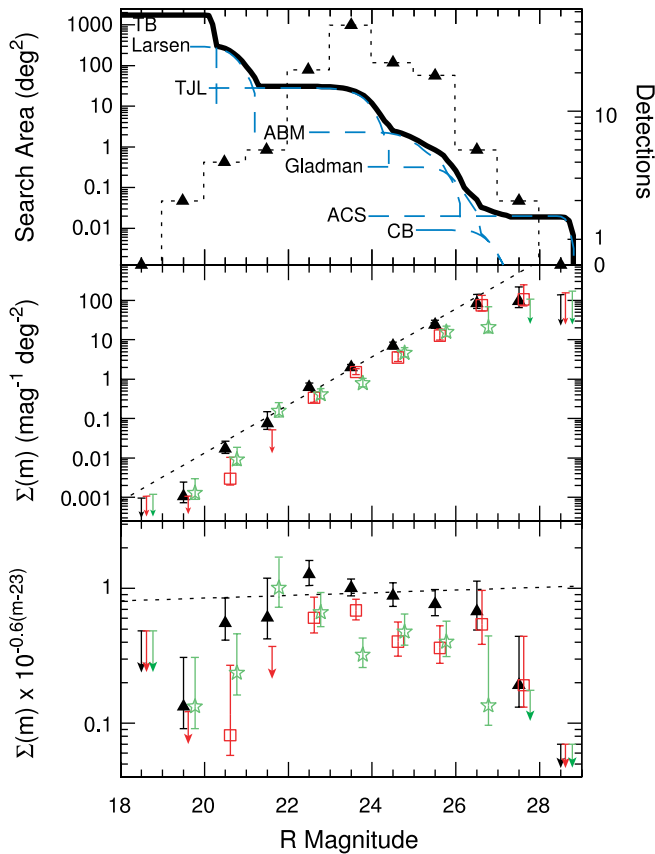
survey over solid angle Ω in a small magnitude interval ΔR is

$$\Delta N = \Sigma(R)\Omega\,\Delta R. \qquad (4)$$

The Appendix is a detailed explanation of the form of the likelihood L of observing TNOs at a set of magnitudes $\{m_i\}$ given an assumed $\Sigma(R)$. This is in general complex if the details of light curves, photometric errors, color corrections, and detection probability must be considered. The Appendix demonstrates that it is safe to take a simplified approach that ignores many of these details, which we present here.

The true surface density $\Sigma(R)$ must be convolved with the color conversion to the observed-band magnitude m, the measurement error on m due to noise and variability, the detection efficiency, and any inhomogeneities of the survey, leaving us with a function $g(m)$ that describes the expected distribution of measured magnitudes in this survey. The expected number of detections from some particular survey is

$$\bar{N} = \int dm\,g(m) = \int dR\,\Omega\eta(R)\Sigma(R), \qquad (5)$$

where $\eta(R)$ is the detection probability for a TNO of mean magnitude R that lies within the geometric area Ω of the survey. This quantity can be determined from Monte Carlo tests.

The likelihood of observing a set of N magnitudes $\{m_i\}$ under an assumed distribution $g(m)$ is

$$L(\{m_i\}|g) \propto e^{-\bar{N}}\prod_{i=1}^{N}g(m_i). \qquad (6)$$

In this work, we will make the approximation that the difference between the observed magnitude m_i and the true R magnitude is minimal (aside from a constant color term) so that we may approximate

$$g(m) \rightarrow \Omega\eta(m)\Sigma(m) \equiv \Omega_{\mathrm{eff}}(m)\Sigma(m), \qquad (7)$$

which implies

$$L(\{m_i\}|\Sigma) \propto e^{-\bar{N}}\prod_{i=1}^{N}\Omega_{\mathrm{eff}}(m_i)\Sigma(m_i), \qquad (8)$$

$$\bar{N} = \int dm\,\Omega_{\mathrm{eff}}(m)\Sigma(m). \qquad (9)$$

When fitting alternative forms of $\Sigma(R)$ to the survey data, the one that maximizes the likelihood in equation (8) (times any prior probability on the models) is the Bayesian preferred model. Confidence intervals on the parameters of the underlying $\Sigma(R)$ can be derived from this probability function as well. We will always take the prior distributions to be uniform, with the exception that the overall normalization of Σ has a logarithmic prior.

Fig. 3.—*Top*: Total effective survey area (*left axis*) within $\pm3^\circ$ invariable latitude vs. magnitude, both summed (*solid curve*) and for individual surveys (*dashed curves*). The histogram shows the number of detected TNOs for the combined surveys (*right axis*). *Middle*: Binned estimate (Bayesian expectation and 68% credible range) of the differential TNO surface density near the invariable plane. Triangles are for the full TNO sample, squares (*red*) are for the CKBO sample, and stars (*green*) are the Excited sample. The latter two are slightly displaced horizontally for clarity. The dashed line is the best single power-law fit to the older data. *Bottom*: Binned surface density relative to an $\alpha = 0.6$ power law (same symbols), i.e., the Σ_{23} values from a stepwise fit to eq. (11). The departure of all samples from a simple power law is clear. This plot is also useful in that the vertical axis is the mass per magnitude interval, if the albedo, material density, and distance are independent of magnitude.

and "scattered disk" TNOs can also slip into the CKBO category under some conditions, and Centaurs near aphelion may be accepted as either CKBOs or Excited TNOs. Of the objects classed as CKBOs in this study, 39 have sufficiently long arcs to determine a and e. Of these, all have 42 AU $< a < 48$ AU and $e < 0.2$ except the $R = 20.9$ Centaur 1995 SN$_{55}$ and the scattered $R = 23$ object 1999 RU$_{214}$.

Of the 33 objects with well-known a in our Excited class, all have $a > 33$, though a few are Neptune-crossing and might be labeled Centaurs by some authors' criteria. Therefore, if these 72 objects with good orbits are a guide, a few percent of all objects would be classified differently if full orbital elements were used instead of just d and i.

3.2. Statistical Methods

We wish to ask what forms for the differential surface density $\Sigma(R) \equiv dN/dR\,d\Omega$ are most consistent with the collected survey data. Note that throughout this paper we will consider the *differential* distribution with magnitude instead of the *cumulative* distribution that is fitted in most previous works. The expected number of detections from a perfect

3.2.1. Goodness of Fit

We will be producing models for $\Sigma(m)$, and hence $g(m)$, that best fit the data. We then ask whether the observations are in fact consistent with having been produced by this model. The general approach is to define some statistic S and ask whether the measured S is consistent with the range of S produced by realizations of the model. We will test goodness of fit with two

TABLE 3
BEST-FIT DIFFERENTIAL SURFACE DENSITY MODELS

	ROLLING POWER LAW					DOUBLE POWER LAW					
SAMPLE	α	α'	Σ_{23}[a]	$P(\leq L)$	Q_{AD}	α_1	α_2	R_{eq}	Σ_{23}[a]	$P(\leq L)$	Q_{AD}
TNO	0.66	−0.05	1.07	0.18	0.55	0.88	0.32	23.6	1.08	0.16	0.12
CKBO	0.75	−0.07	0.53	0.54	0.04	1.36	0.38	22.8	0.68	0.71	0.23
Excited	0.60	−0.05	0.52	0.04	0.06	0.66	−0.50	26.0	0.39	0.24	0.13

[a] Number per magnitude per square degree.

statistics. The first is simply the likelihood $L(\{m_i\}|\Sigma)$ itself, given in equation (6). The probability $P(\leq L)$ of a realization of the model having lower likelihood than the measurements will be calculated by drawing random realizations from the best-fit distribution. Values $P < 0.05$ or $P > 0.95$ are signs of a poor fit.

We also use the Anderson-Darling (A-D) statistic, defined as

$$AD = \int \frac{[S(m) - P(m)]^2}{P(m)[1 - P(m)]} dP(m) \qquad (10)$$

(Press et al. 2002). Here $P(m)$ is the cumulative probability of a detection having magnitude $\leq m$, so $0 \leq P \leq 1$. The cumulative distribution function of the observed objects is $S(m)$. The A-D statistic is related to the more familiar Kolmogorov-Smirnov (K-S) statistic, which is the maximum of $|S(m) - P(m)|$, but is more sensitive to the tails of the distributions. We calculate Q_{AD}, the probability of a random realization having *higher* AD-value than the real data. Values of $Q_{AD} < 0.05$ indicate poor compliance with the model distribution.

Because the likelihood and AD-values of the real data are calculated from a $g(m)$ that is the best fit to the data, it is necessary to also fit each random realization before calculating L or AD. Because the normalization of g is always a free parameter, we fix each random realization of $g(m)$ to have the same number of detections as the real data.

We note further that we always sum the effective areas and detections of all surveys before analyzing the data, rather than considering the likelihood of each component survey. We believe this makes the fit a little more robust to small errors in individual surveys' detection-efficiency estimates. In § 3.7, we examine whether each constituent survey is consistent with the $\Sigma(R)$ derived from the full data set.

3.3. *Single Power-Law Fits*

Previous fits to the magnitude distribution of TNOs have assumed that the cumulative, and hence differential, distribution fits a single power law. We attempt to fit the ACS and previous survey results to a differential distribution of the form

$$\Sigma(R) = \Sigma_{23} 10^{\alpha(R-23)} \; \text{deg}^{-2}. \qquad (11)$$

We first fit this law to the older surveys, excluding the ACS and TB data. We recover a best fit of $\alpha = 0.61 \pm 0.04$ for the TNO sample, which is consistent with the previous fits, for example, TJL. This best-fit power law is a marginally acceptable fit to the data, with likelihood probability $P(\leq L) = 0.92$ and A-D probability $Q_{AD} = 0.06$.

When we include the ACS and TB data in the power-law fit, we find that the best-fit slope drops to $\alpha = 0.58 \pm 0.02$. The fit is strongly excluded, however, with $P(\leq L) = 0.997$ and $Q_{AD} \leq 0.001$. The probability of detecting so few objects in the ACS survey under this power law is $P(\leq N) < 10^{-14}$, and the TB survey is also highly deficient. A single power law extending to the ACS data is ruled out at very high significance, as expected. By contrast, there is a 16% probability of finding three or fewer TNOs in the ACS survey under the best-fit double power-law $\Sigma(m)$ (§ 3.6).

3.4. *Binned Representation*

Figure 3 presents a nonparametric, binned estimate of the differential surface density. The survey data for each 1 mag interval over the range $18 < R < 29$ are fitted to the form given by equation (11), with α fixed to 0.6 and Σ_{23} free. The expectation $\bar{\Sigma}_{23}$ and the 68% Bayesian credible regions are calculated as described in § A.2.2. The middle panel shows the resulting expectation of Σ at the center of each bin, and the bottom panel plots the $\bar{\Sigma}_{23}$ values, that is, the deviation of each bin from a pure $\alpha = 0.6$ power law. This plot is useful for visualizing the departures from power-law behavior, but we always fit models to the full survey data rather than the binned version. It is immediately apparent that the TNO surface density departs from a single power law at both the bright and faint ends of the observed range, for both the CKBO and Excited subsamples.

3.5. *Rolling Power-Law Fits*

As a next level of complication, we consider a surface density with a rolling power-law index:

$$\Sigma(R) = \Sigma_{23} 10^{\alpha(R-23) + \alpha'(R-23)^2}. \qquad (12)$$

Note that this is a lognormal distribution in the flux, roughly so for diameter as well.

This fit to the full TNO sample is now acceptable, with $Q_{AD} = 0.55$ and $P(\leq L) = 0.18$. The CKBO and Excited samples are only marginally well fitted, with Q_{AD} values of 0.04 and 0.06, respectively. Best-fit parameters are given in Table 3, and the best-fit $\Sigma(R)$ are plotted over the data in Figure 4.

The addition of the single parameter α' to the single power-law fit leads to highly significant improvements in the likelihood: $\log L$ is increased by 32, 22.2, and 12.6 for the TNO, CKBO, and Excited samples, respectively. This is equivalent to $\Delta \chi^2 = 2 \Delta(\log L) \geq 25$ for one additional parameter, which has negligible probability of occurring by chance. Hence the single power-law fits are strongly excluded.

Using the Bayesian approach of § 3.2, we may produce a probability function $P(\Sigma_{23}, \alpha, \alpha'|\{m_i\})$ given the observations.
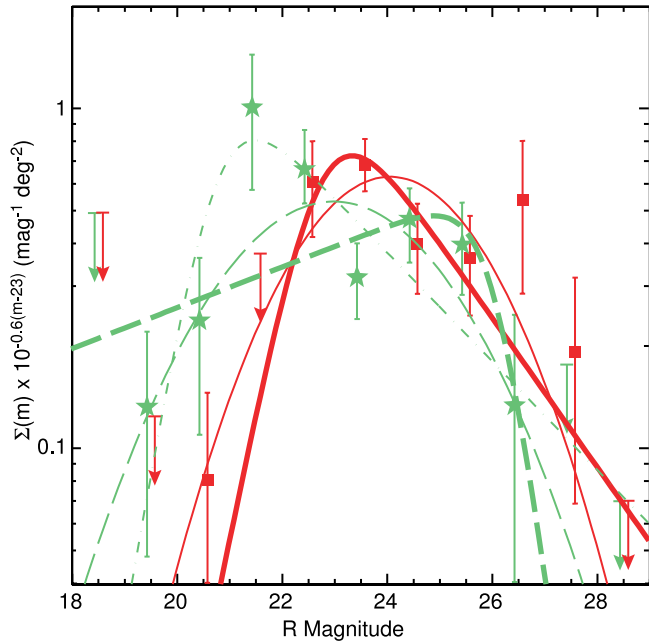
FIG. 4.—Best-fit models for the differential surface density $\Sigma(R)$ of TNOs plotted along with the binned representation of the data from Fig. 3. The stars (*green*) are binned data for the Excited sample, and squares (*red*) are the CKBO sample, and we have again divided out the function $10^{0.6(R-23)}$. The two thick curves are double power-law fits, and the two thin curves are rolling-index power laws. Solid curves (*red*) are for the CKBO sample, and dashed (*green*) are for the Excited sample. The dash-dotted curve is a secondary double power law fit to the Excited sample that is consistent with these data but inconsistent with the existence of Quaoar-sized objects (or Pluto). The precipitous drop in the best-fit double power laws at the bright (CKBO) and faint (Excited) ends is an artifact of the absence of detections in this sample. There are less precipitous drop-offs that are quite consistent with the data, as is apparent from Fig. 6.
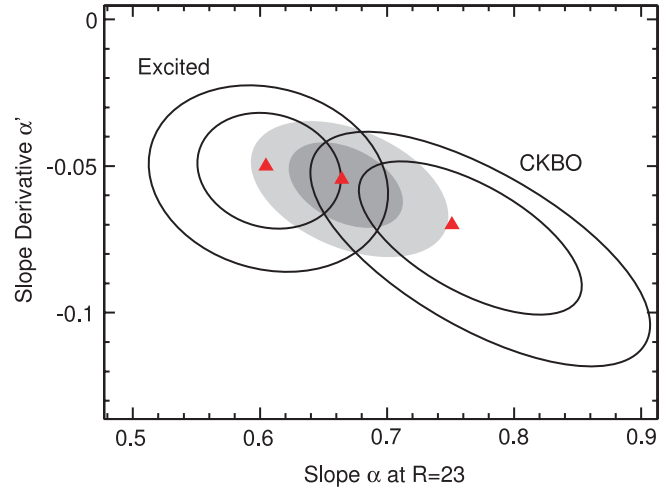

FIG. 5.—Allowed ranges of the slope and derivative for rolling power-law fits to the sky density of TNOs, as per eq. (12). Shaded regions are for the full TNO sample, while contours are for the CKBO and Excited subsamples. In all cases, contours enclose 68% and 95% of the total posterior density. The curvature α' of $\Sigma(R)$ is clearly nonzero, and the two dynamical subsamples are distinct. The lower α for the Excited sample implies that its mean magnitude and mass are larger than those of the CKBOs.

Figure 5 plots the credible regions for α and α' in the three samples. Note first that $\alpha' = 0$ is strongly excluded, that is, a rolling index is required. For the rolling-index model, any $\alpha' < 0$ gives convergent integrals for TNO number and mass at both bright and faint ends. Second, we see that the CKBO sample requires a larger α, meaning that $\Sigma(R)$ is steeper at $R = 23$ than for the Excited sample, that is, the CKBO sample is shifted to fainter magnitudes relative to the Excited sample, by about 1 mag. In the next section we will discuss the implications of this magnitude shift.

3.6. Double Power-Law Fits

We next consider a surface density that is the harmonic mean of two power laws:

$$\Sigma(R) = (1 + c)\Sigma_{23}[10^{-\alpha_1(R-23)} + c10^{-\alpha_2(R-23)}]^{-1}, \quad (13)$$

$$c \equiv 10^{(\alpha_2-\alpha_1)(R_{eq}-23)}. \quad (14)$$

Under the convention $\alpha_2 < \alpha_1$, the asymptotic behavior of this function is a power law of indices α_1 at the bright end and α_2 at the faint end, with the two power laws contributing equally at R_{eq}. The free parameters for this model are $\{\alpha_1, \alpha_2, R_{eq}, \Sigma_{23}\}$. We introduce the double power-law model for two reasons: First, in the next section we will be interested in how strongly the parameterization of $\Sigma(R)$ affects our conclusions, so we want some alternative to the rolling-index model. Second, some models for accretion and erosion of

planetesimals predict asymptotic power-law behavior, which is absent in the rolling-index model.

The double power-law model adequately describes the TNO, CKBO, and Excited samples, with $Q_{AD} \geq 0.12$ and $P(\leq L) \geq 0.16$. The best-fit parameters are listed in Table 3 and plotted with the binned representation of the data in Figure 4.

The values of $\log L$ for the double power-law fits are within ± 1.3 of those for the rolling power-law fits. So while the double power law is clearly superior to the single power law, the likelihood itself offers no preference over the rolling power law. The A-D statistic is, however, more acceptable for the double than for the rolling power-law fits to the CKBO and Excited samples (Table 3). There is weak statistical preference and theoretical prejudice for the double power laws; in § 4.2, we note that the rolling power-law fits do not properly describe the number of very bright Excited TNOs found away from the invariable plane.

In Figure 6, we plot the Bayesian posterior distribution $P(\alpha_1, \alpha_2)$ for the double power-law fits to the various samples after marginalization over the less interesting variables Σ_{23} and R_{eq}. We also plot the projections onto the single variables α_1 and α_2 for the CKBO and Excited subsamples. Note that we have applied a prior restriction $-0.5 < \alpha_i < 1.5$, as we consider the more extreme slopes to be unphysical.

Several features of the (α_1, α_2)-constraints are noteworthy. First, the CKBO and Excited samples once again appear to be distinct, except that the 95% confidence level (CL) region for the Excited sample has a tail at $(\alpha_1 > 0.8, \alpha_2 \approx 0.4)$ that contains 10% of the posterior density and overlaps the CKBO region of viability. Fits in this secondary range predict very few Excited TNOs at $R < 19$, which is consistent with our limited sample, but inconsistent with the membership of Pluto, Quaoar, or 2004 DW in the Excited class. If we include in our likelihood function a prior equal to the probability that each model produces at least one Excited TNO at $R \leq 18.5$ (the "Quaoar prior"), then this long tail disappears from the Excited credible region (as illustrated by the dot-dashed lines in Fig. 6). We further discuss the CKBO-Excited dichotomy in § 3.8.
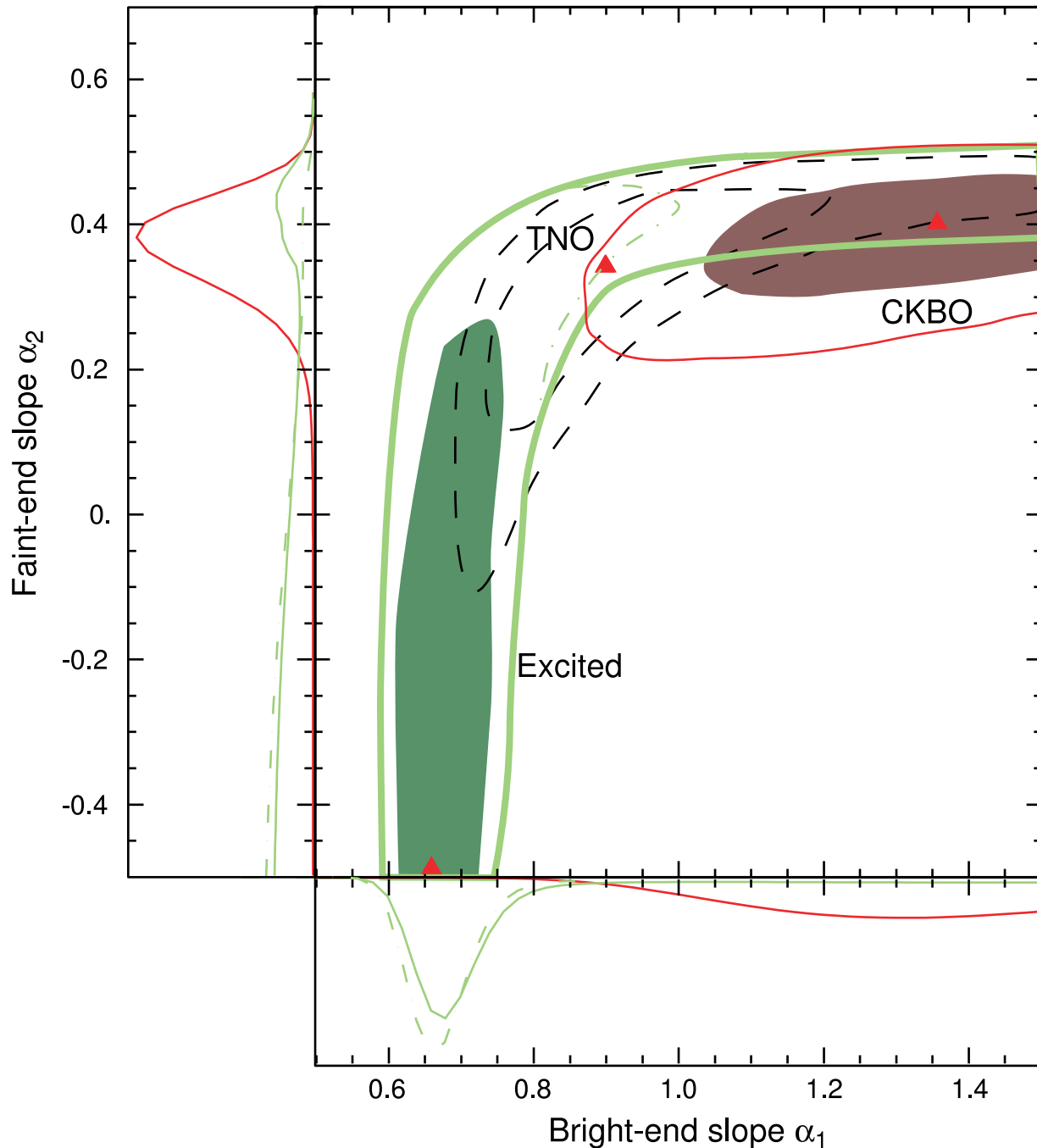
Fig. 6.—Allowed ranges of the two slopes for double power-law fits to the differential surface density of TNOs, as per eq. (13). Shaded regions enclose 68% of posterior probability for the CKBO and Excited subsamples (*red and green, respectively*), with outer solid contours bounding 95% regions. The dashed contours are for the full TNO sample. Along the horizontal and vertical axes are the projected one-dimensional distributions of each slope. The two dynamical classes have distinct magnitude distributions, with the exception of the high-α_1 tail on the outer Excited contour. If we include a prior constraint that the Excited class contain one object on the sky with $R \leq 18.5$ (the "Quaoar prior"), we obtain the dot-dashed contours instead. The bright-end slope of the CKBO group is likely steeper than the Excited class, and the faint-end slope of the Excited class is probably shallower.

For any $\alpha_2 < 0.6$, the mass integral converges at the faint end (§ 4.1), and this is satisfied at high confidence for all samples. The faint-end slope of the CKBOs is well constrained at 0.38 ± 0.12 (95% CL). The faint-end slope of the Excited class is poorly determined, with only a bound $\alpha_2 \lesssim 0.36$ (95% CL with the Quaoar prior). The absence of Excited TNOs in the ACS survey leads to this degeneracy.

For $\alpha_1 > 0.6$ the bright-end mass converges, and this is satisfied at 95% confidence for the Excited subclass and at very high confidence for the CKBO sample. The bright-end slope for the Excited class is $0.66^{+0.14}_{-0.08}$ (95% CL with Quaoar prior), while the absence of bright CKBOs leads only to a bound of $\alpha_1 \gtrsim 0.97$ for their asymptotic index.

The CKBOs certainly seem to have a steeper bright-end slope (fewer large objects) than the Excited objects, and there is less secure evidence that the Excited class has a shallower faint-end slope (fewer small objects). There is thus evidence of different accretion and erosion histories for these two samples.

3.7. *Internal Consistency*

Before proceeding with further interpretation, we pause to ask whether there are any internal inconsistencies among the collected survey data. We check the surveys individually for consistency with the best-fit double power law.

We will make use of three consistency tests. The first is simply the number N of detected objects. This probability distribution for N follows the Poisson distribution,

$$P(N|\bar{N}) = \frac{\bar{N}^N}{N!} e^{-\bar{N}}. \tag{15}$$

and the cumulative probability $P(\leq N)$ of having detected N or fewer objects is also easily calculated. The drawback of the Poisson test is that it makes no use of the distribution of magnitudes within a survey.

The second statistic that we use is the Q_{AD} statistic described above, which has the disadvantage that it discards information on the total number of detected TNOs. The third statistic we will use is a form of log-likelihood:

$$\mathcal{L}(\{m_i\}|g) \equiv N \log \bar{N} - \log N! - \bar{N} + \sum_{i=1}^{N} \log\left[\frac{g(m_i)}{\bar{g}}\right], \tag{16}$$

$$\log \bar{g} \equiv \frac{\int g \log g \, dm}{\int g \, dm}. \tag{17}$$

This statistic is useful in that it is the logarithm of L in equation (6) when the model and number of detections N are fixed. The expectation value of $\mathcal{L}$ when N is held fixed is also equal to the logarithm of the Poisson probability in equation (15). This statistic hence has sensitivity to both the number and distribution of detections in a survey under test. For any given model and survey, we can generate 1000 or more Monte Carlo realizations to calculate the probability $P(\leq \mathcal{L})$ of the measured likelihood being generated by chance under the model.

When comparing a constituent survey with the full-data fits, we do not refit each realization, because individual surveys do not heavily influence the overall fit.

The results of the three statistical tests for each survey are given in Table 2. The only sources of tension, marked in boldface in the table, are for the Larsen et al. survey, which contains too many objects at 97% CL, and the Gladman et al. survey, which is overabundant at 98% CL. The A-D tests also indicates that the Larsen et al. survey is too skewed toward faint objects ($Q_{AD} = 0.05$), and the Gladman et al. detections are also too skewed toward faint objects ($Q_{AD} = 0.03$). Chiang & Brown were also slightly lucky to find two objects in their 0.01 deg^2 survey, if the collective fit is correct.

These excursions are worse than we would expect from Poisson statistics, but not horribly so: with three statistical tests for each of seven surveys, we expect approximately one to show a discrepancy at better than 95% significance, while we have two surveys discrepant at this level. There is no justification for excluding any particular survey data. For example, consider the fact that the ABM and Gladman et al. surveys are in poor agreement in the $25 < R < 26$ magnitude range. The Gl sky density in this bin is 3 times that of ABM. The odds of obtaining by chance a disparity this large given the number of detections in the survey are approximately 1%. Since we have overlap between different surveys in several of our bins, the chance of our having found one such discrepancy

between any two surveys in any of our bins is perhaps 5%. The discrepancy is hence worrisome but not outrageous.

It is possible that either ABM overestimate their completeness or Gladman et al. have some false positive detections at their faint end. There are no obvious flaws to either work—ABM have a thorough artificial-object estimate of efficiency, and Gladman et al. detect each object on two consecutive nights. In the absence of any reason to reject either data set, we will continue to sum the effective areas and total detections of both surveys. We have verified that none of our conclusions are significantly affected by omission of either data set.

Further data in this magnitude range are clearly desirable, as it helps define the departure of the faint end from a power-law slope. Surveys at $25 < R < 26$ require long integrations on large telescopes with large-area CCD mosaics. Such efforts are underway, using, for example, the VLT (O. Hainaut 2002, private communication) and Subaru Telescope (D. Kinoshita 2002, private communication).

3.8. *Dynamical Subclasses*

The parametric $\Sigma(R)$ fits to the CKBO and Excited subclasses appear to differ, though the evidence is not yet ironclad. Since the CKBO and Excited subclasses have the same effective area at a given magnitude, we may apply a two-sample A-D test to see if their magnitudes are drawn from the same distribution. We obtain $Q_{AD} = 0.039$, *rejecting at 96% confidence the hypothesis that the CKBO and Excited TNOs have identical magnitude distributions.* The largest difference in the magnitude distributions is the lack of bright CKBO members, which is noted by Trujillo & Brown (2003) and discussed in detail below. Nearly all the statistical significance of the result arises from the TJL sample. The test indicates that there are (at least) two distinct size distributions in the TNO population, and hence the magnitude distribution should be fitted by dynamical class rather than summed.

Our division into dynamical classes is crude because of incomplete orbital elements (§ 3.1), which can only have ameliorated the distinction between the two size distributions. A more precise division may yield even more pronounced size differences between dynamical classes.

4. INTERPRETATION

4.1. *The Mass Budget of the Kuiper Belt*

The detection of departures from a single power law now make it possible to estimate the total TNO mass without any divergences. The total mass of a TNO population may be expressed as

$$M_{tot} = \sum_{TNOs} M_i \tag{18}$$

$$= M_{23} \Omega \int dR \, \Sigma(R) 10^{-0.6(R-23)} f^{-1}$$

$$\times \left\langle \left(\frac{p}{0.04}\right)^{-3/2} \left(\frac{d}{42 \text{ AU}}\right)^6 \left(\frac{\rho}{1000 \text{ kg m}^{-3}}\right) \right\rangle, \tag{19}$$

$$M_{23} = 7.8 \times 10^{18} \text{ kg}. \tag{20}$$

The surface density Σ is the mean over solid angle Ω of the sky, and f is the fraction of the TNO sample at magnitude R that lies within the area Ω. The material density, albedo, and heliocentric distance are ρ, p, and d, and M_{23} is the mass of a TNO that has $R = 23$ with the given canonical albedo, density,

and distance. We ignore the effects of illumination phase, heliocentric versus geocentric distance, and asphericity. The angle brackets indicate an average over the TNOs at the given magnitude. We make the usual bold assumption that the bracketed quantity is independent of apparent magnitude and hence can be brought outside the integral in equation (19). We will carry out the integral over $14 < R < 31$.

4.1.1. The Mass of the Classical Kuiper Belt

The approximation of a common heliocentric distance is workable for the CKBO sample, which by definition ranges over $38 \text{ AU} < d < 55 \text{ AU}$. Of the nearly 1000 TNOs detected to date, none are known to have low-inclination, low-eccentricity orbits with semimajor axis $a > 50 \text{ AU}$ or $a < 38 \text{ AU}$. A sharp decrease in surface density beyond 55 AU is apparent even after correction for selection effects (Allen et al. 2001; TJL; Trujillo & Brown 2001). It is therefore physically meaningful to consider our CKBO sample to represent a dynamical class that is largely confined to heliocentric distances of 42 AU ± 10%.

For the CKBO sample, the value of the integral is $2.85 \text{ deg}^{-2} \pm 15\%$ (95% CL) when marginalized over the double power-law fits. The value when using the rolling-index form for $\Sigma(R)$ is indistinguishable, so we believe this to be robust to parameterization. The solid angle over which Σ has been averaged is $360° \times 6°$. Because the CKBO sample is by definition restricted to $i < 5°$, the residence fraction f is high—unity for $i < 3°$, and 0.83 if the inclinations are uniformly distributed between $0°$ and $5°$. We will take $f = 0.9$ and ignore any uncertainty, as it will be small in comparison with that of the albedo and density terms. We then obtain (at 95% CL)

$$M_{\text{CKB}} = (5.3 \pm 0.9) \times 10^{22} \text{ kg}$$
$$\times \left(\frac{p}{0.04}\right)^{-3/2} \left(\frac{d}{42 \text{ AU}}\right)^6 \left(\frac{\rho}{1000 \text{ kg m}^{-3}}\right). \quad (21)$$

The prefactor is now determined to much greater accuracy than the scaling constants. The CKBO mass is nominally equal to just $0.010 \, M_\oplus$, or a mere 4 times the mass of Pluto (8 times, if the CKBOs share Pluto's density of 2000 kg m^{-3}).

TJL report an estimated mass for CKBOs with diameters in the range $100 \text{ km} < D < 2000 \text{ km}$ of $\approx 1.8 \times 10^{23}$ kg, under the same assumptions about density and albedo as made here. We would naively expect our estimate to be larger, not 3 times smaller, than the TJL estimate, because we now include bodies smaller than 100 km—though the ACS data show that these smaller bodies hold a minority of the mass. The discrepancy is in part attributable to our more restrictive definition of the classical belt: we require $i < 5°$ whereas TJL demand only $41 \text{ AU} < a < 46 \text{ AU}$ and $e < 0.25$. The larger part of the discrepancy is due to our conclusion that the CKBO population has $\alpha > 0.6$ for $m \lesssim 24$, greatly reducing the mass that TJL's $\alpha \approx 0.6$ places in large objects.

Gladman et al. (2001) estimate the mass of TNOs in the 30–50 AU range to be 0.04–$0.1 \, M_\oplus$ (for unspecified material density), if the size distribution turns over to the Dohnanyi slope for $D \sim 40$ km. Our new value remains below this estimate even if we allow for the fact that the Excited TNOs contribute a similar mass density to the CKBOs in this distance range (next subsection), again reflecting the fact that the present data fall below the assumed power laws at both large and small object sizes.

4.1.2. The Mass in Excited TNOs

The TNOs in our Excited sample—a mixture of resonant and high-excitation nonresonant orbits—are drawn from dynamical families whose radial and vertical extent remains quite uncertain. In particular, our selection effects for the so-called scattered-disk objects are poorly known. Our estimates of the total mass will therefore be much less secure than for the CKBO population.

The assumption that the bracketed quantity in equation (19) is independent of magnitude is dubious for the Excited class, because it is likely that the brighter bins are biased toward objects near perihelion, which can be an extreme bias for a scattered-disk member. We proceed nonetheless. The integral over the double power-law $\Sigma(R)$ is well determined: marginalizing over the fitted parameters we obtain $3.5 \pm 1 \text{ deg}^{-2}$ for the double power law, somewhat lower for the rolling-index fit.

Because the excited population has high inclinations, the residence fraction f will be smaller; if the inclinations i are distributed as a Gaussian with $\sigma_i = 10°$, then they spend on average $f \approx 0.5$ of their time within $3°$ of the invariable plane. The inclination distribution is, however, poorly known, especially under our definition of the Excited sample.

The mean distance appears as d^6 and is highly uncertain for the "scattered disk" objects, but it is sensibly bounded for Plutinos. An upper bound on the Plutino mass comes from assuming that the Excited class contains most of the Plutinos that are closer than 39 AU to the Sun, or very crudely half of the total Plutino population. The brighter surveys are biased against Plutinos that are currently beyond their semimajor-axis distance, and under our definition of the CKBO sample, Plutinos at low inclination beyond 38 AU will be put into the CKBO class. So we will calculate a total mass for the detectable Excited sample assuming $d = 39 \text{ AU}$ and double it to bound the Plutinos. Following this procedure, we obtain

$$M_{\text{Plutino}} \lesssim 1.3 \times 10^{23} \text{ kg } (p/0.04)^{-3/2}$$
$$\times \left(\frac{d}{39 \text{ AU}}\right)^6 \left(\frac{\rho}{1000 \text{ kg m}^{-3}}\right) \left(\frac{f}{0.5}\right)^{-1}. \quad (22)$$

An estimate for the so-called scattered-disk population is even less certain given the potentially large values of $\langle d^6 \rangle$ (even though no detected objects yet exceed $d \sim 60 \text{ AU}$).[5] Taking the mean d to be 42 AU and $f = 0.5$ gives an Excited-class mass of 1.3×10^{23} kg. It perhaps suffices to estimate that the Excited sample is comparable to or several times the mass of the CKBOs, because the surface density integrals are nearly equal, the residence fraction f is lower for the Excited objects, and the mean d^6 factor could be larger for the Excited class. The value here is, however, a fair estimate of the Excited mass *within* 50 AU.

It thus appears that Pluto itself accounts for $\gtrsim 10\%$ of the mass of the Plutino population, and perhaps of the entire Excited population. We will investigate this further in § 4.2.

TJL crudely estimate the number of $D > 100 \text{ km}$ objects with scattered-disk orbits to be comparable to the CKBOs, and the Plutinos to be ~ 20 times less abundant. The absence of Plutinos in the ACS data suggests that the Plutinos also have a break in $\Sigma(R)$ such that little of their collective mass is in

---

[5] We do not include the newly discovered object Sedna, at $d = 90 \text{ AU}$, in the scattered disk, given its perihelion at 76 AU.

small objects, but we do not attempt a further quantitative bound. If this TJL estimate is correct, then Pluto dominates the Plutino mass and is several to tens of percent of the scattered-disk mass.

4.2. *The Largest Objects in the Dynamical Classes*

We examine here some implications of the large-size behavior of our fitted $\Sigma(R)$ functions. These results are not, of course, a direct consequence of the new small-end ACS data, except insofar as the latter make it clear that single power-law fits to the full population should not be expected to properly characterize the bright end. The results of this section flow from our efforts to create a homogeneous subsample of all the published brighter surveys.

The double power-law fits to the CKBO sample favor a bright-end slope that is significantly steeper than for the Excited sample. If correct, this implies a different accretion history for the two classes, since it is believed that erosion should not have affected the largest TNOs (Stern 1996). It would also imply that the brightest (and largest) member of the Excited class will be significantly larger than the largest CKBO, and that the Excited sample will have a substantial fraction of its mass in the largest objects (since $\alpha_1 \approx 0.6$) while the CKBO sample will not. A possible preference for large objects to reside in high-excitation populations has been suggested before in studies of less well controlled samples (Levison & Stern 2001) and in theoretical studies (Gomes 2003) and is verified by the TB survey.

We have inferred the bright-end slope difference by using only the subset of survey data to date that has invariable latitude below $3°$ and has published survey statistics. We may check the accuracy of our inferences by some comparisons with the full sample of nearly 1000 TNOs that have been discovered to date, as listed on the Minor Planet Center (MPC) Web pages 2003 July.

We first ask what should be the brightest TNO on the full sky if extrapolation of our fitted double power-law $\Sigma(R)$ were to correctly describe all TNOs. We may calculate the probability distribution for the magnitude of the brightest TNO by marginalizing over all our double power-law fits and assuming an available area of sky equal to Ω/f, using the values estimated above. To be specific, we calculate

$$P(N(<R) = 0)$$

$$= \int d\boldsymbol{p}\, P(\boldsymbol{p}|\{m_i\}) P(N(<R) = 0|\boldsymbol{p}) \qquad (23)$$

$$= \int d\boldsymbol{p}\, P(\boldsymbol{p}|\{m_i\}) \exp\left[-\frac{\Omega}{f} \int_0^{m'} dm'\, \Sigma(m'|\boldsymbol{p}) \right]. \qquad (24)$$

Here $\boldsymbol{p}$ is a vector of parameters for Σ, $P(\boldsymbol{p}|\{m_i\})$ is the normalized Bayesian posterior probability for the model parameters given the observed data, and $\Omega = 360° \times 6°$ is the total area of the low invariable latitude strip on the sky.

Figure 7 shows our estimated probability of there being, somewhere on the sky, a TNO brighter than a given R magnitude. For the CKBOs, the double and rolling power-law fits are in general agreement. The median expected magnitude for the brightest CKBO on the sky is 20.3 mag. The brightest TNO found to date that meets our CKBO criteria is 2002 KX_{14}, at $R = 20.6$, which is found by the TB survey but was not used in our analysis since it is below our adopted 20.2 mag cutoff. Nearly all the sky within $5°$ of the invariable plane has

been surveyed for such bright objects, by Trujillo & Brown (2003) and/or the Southern Edgeworth-Kuiper Belt Survey (Moody et al. 2003), with all discoveries having been transmitted to the MPC. Hence it is unlikely that a CKBO significantly brighter or larger than 2002 KX_{14} exists on the sky. The fitted and extrapolated $\Sigma(R)$ models suggest a 70% chance of finding a CKBO brighter than 2002 KX_{14}, so it would be acceptable for 2002 KX_{14} truly to be the largest CKBO (or nearly so).

For the Excited class an extrapolation is more speculative, since a smaller fraction of the available sky has been surveyed, and we include in our analysis only a fraction of the surveyed area. The median expected magnitude of the brightest Excited TNO is 18.4 for the double power-law and 19.0 for the rolling-index fits. The brightest TNO is Pluto, which would have $R = 17.5$ if it had our assumed albedo of 0.04 (Buratti et al. 2003), or $R = 16.5$ if the albedo is 0.10, comparable to Quaoar (Brown & Trujillo 2004). Under the double power-law fits, there is a 4%–17% chance of finding an Excited TNO this bright, so it is feasible to consider Pluto to have been produced by the same physical process as the other TNOs. Under the rolling-index model, however, the odds of a Pluto on the sky are less than 2%; hence, under this model we would have to consider Pluto as an exceptional object with a distinct formation mechanism from the other TNOs. The largest and brightest TNO outside the Pluto-Charon system is Quaoar at $R = 18.5$—also discovered by Trujillo & Brown but outside the bounds of our $\pm 3°$ swath—which at $i = 8°$ would be excluded from our CKBO sample. From the figure we see that if the bright end follows a power law, we would expect the largest Excited TNO to be in the Quaoar–Pluto range. So we again find that the largest objects known to date are consistent with extrapolation of our double power-law $\Sigma(R)$ fits—or with the rolling-index model, if we consider the Pluto-Charon system as exceptional.

The degree of dominance of the brightest known objects is also consistent with our double power-law fits to our selected subsample. The 10 brightest known CKBOs have $20.6 < R < 21.8$ and contribute $\approx 2\%$ of the estimated CKB mass (assuming common albedo and material density). Again, surveys for low-inclination TNOs this bright are now majority-complete, so this fraction is not likely to evolve much. Hence, the largest objects in the CKB do *not* hold a significant fraction of its mass, confirming the validity of the $\alpha_1 > 0.85$ bright-end slope.

The 10 brightest known resonant/scattered TNOs, excluding Pluto and Charon, have $18.5 < R \lesssim 20.5$. Their combined mass, with canonical albedo and density, is 1.3×10^{22} kg, roughly equal to Pluto's mass, and roughly 10% of the total estimated Excited-family mass. Thus, the largest bodies known hold tens of percent of the known Excited-class mass, confirming that the power-law slope is near 0.6.

The conclusions we have drawn from our controlled TNO subsample are therefore supported by analysis of the total sample of known bright TNOs. In particular, we find that the Excited class is near the $\alpha_1 = 0.6$ value with equal mass per logarithmic size bin, while the CKBOs have a steeper $\alpha_1 > 0.85$ that puts less mass in large objects. Under the double power-law model, Pluto is a uniquely but not anomalously large Excited TNO. Since erosion should not have significantly altered the $\gg 100$ km objects in the current trans-Neptunian environment, a simplistic interpretation is that the Excited objects were formed in a region of the solar system that allowed the accretion process to proceed further than in
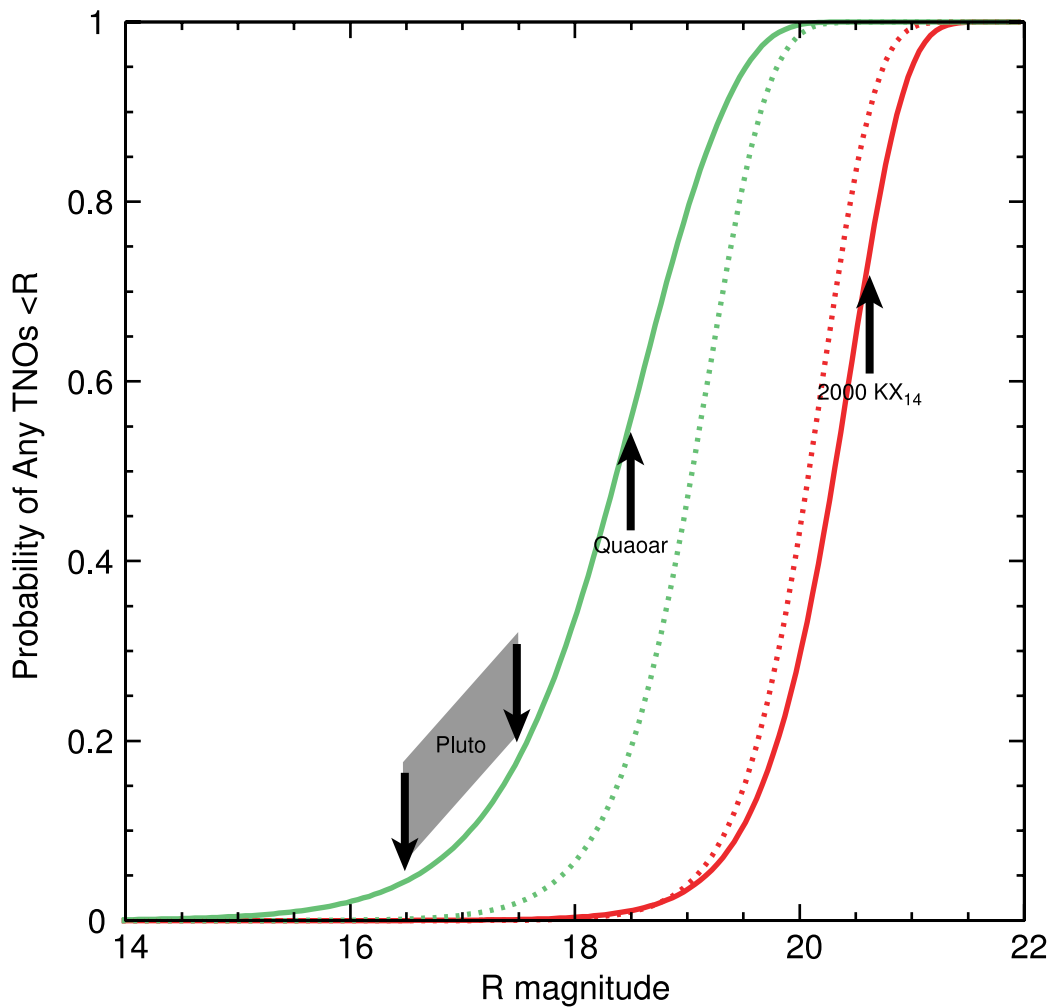
FIG. 7.—Distribution for the brightest expected TNO on the sky, shown vs. R magnitude for the CKBO (*red*; right) and Excited (*green*; left) samples. The plotted quantity is the cumulative likelihood of finding a TNO brighter than R. The solid lines are derived from an extrapolation of the double power-law fits to the invariable-plane surveys collected in this paper, and the dotted lines are for the rolling-index power laws. Given that much of the relevant sky area has now been searched for bright TNOs, we see that the extrapolations of the power laws are consistent with 2000 KX_{14} being the brightest CKBO (or nearly so), and with Pluto or Quaoar being the brightest Excited TNO (Pluto is plotted at the apparent magnitudes it would have with albedo 0.04–0.10). If the rolling-index fit is the proper extrapolation, Pluto has to be considered an exceptional object.

the ~42 AU location of the CKBOs. This is consistent with the scenario in which the Excited TNOs formed in a low-excitation population closer to the Sun (Malhotra 1993, 1995; Gomes 2003), where higher space densities and relative velocities could speed accretion.

4.3. *The Smallest Known TNOs and Erosion History*

Calculations of collision rates and energies suggest that the population of TNOs with $D \lesssim 100$ km has been strongly influenced by collisional erosion. The ACS survey provides the first strong constraints on this population, so in this section we provide some basic comparison of the observed magnitude distribution to models of the accretion and erosion history of the TNOs. Throughout this section we will make the simplifying assumption that the TNO samples we have gathered are at fixed distance with fixed albedo, so that the magnitude distribution may be directly translated into a size distribution. If the magnitude distribution scales locally as $dN/dm \propto 10^{\alpha m}$, then the size distributions will locally follow the common parameterization $dN/dD \propto D^{-q}$ with $q = 5\alpha + 1$. We will prefer the double power-law models for $\Sigma(R)$ to the rolling-

index models for this discussion, as the size evolution models typically predict such behavior.

4.3.1. *Comparison with the MPC Database*

The conclusion that the faint-end $\Sigma(R)$ is shallower for CKBOs than Excited objects does not have exceptionally strong statistical support in our sample, for example, three versus zero detections in the ACS survey. We again look to see if the trend is borne out by the sample of all objects submitted to the MPC. Of the 23 objects with magnitude $H \geq 9.6$ and perihelion $q > 28$ AU, only five would fall into our Excited class. The dominance of CKBOs in this range is significant, given that Excited TNOs dominate the low-H objects and are comparable to CKBOs near $R \approx 23$, discovery of high-H Excited objects is favored because of their nearer perihelia, and several of the $H > 9.6$ Excited TNOs could turn out to be CKBOs once more accurate inclinations are obtained. This test is not independent of our more controlled analysis, because many of the $H > 9.6$ TNOs at the MPC are from the ACS, ABM, and Gl surveys. Nonetheless, the trend in our controlled subsample seems to extend to the full sample.

4.3.2. Equilibrium Collisional Cascades

An analytic description of a collisional cascade is given by Dohnanyi (1969), who derives $q = 3.52$ and $\alpha = 0.50$ for an equilibrium solution. In such a steady state, the loss of objects from a given mass bin due to grinding and catastrophic destruction is exactly replenished by the gain of fragments from collisions on larger bodies. A population of high-mass objects is of course required as a mass reservoir to maintain such an equilibrium. We see from Figure 6 that $\alpha_2 \geq 0.5$ has a low probability of describing either the CKBO or Excited population in the ACS survey: the true distribution is markedly shallower (meaning relatively fewer small bodies) than the canonical Dohnanyi value, particularly in the Excited sample.

The failure of the analytical model could perhaps be ascribed to the particular assumptions in the model, for example, that the size distribution will follow a power law and that the distribution of fragment sizes will take a particular power-law form, although the equilibrium form should be robust as long as the fragmentation law is scale-free. Pan & Sari (2004) suggest that the observed size distribution can be explained by a fragmentation law for rubble-pile objects that is not scale-free. An alternative explanation is that the present-day TNO population is not in collisional steady state. Perhaps we have instead a snapshot of two populations for which the small-body population is continuously decreasing and erosive destruction is very advanced. In the CKB it is not even clear what bodies could serve as a mass reservoir, since the largest bodies hold little of the mass.

4.3.3. Numerical Models: General Results

Modeling of nonequilibrium collisional evolution requires numerical simulation, particularly if coeval accretion is modeled as well. Three groups have produced such models: Durda & Stern (2000) (who estimate body lifetimes but do not follow the long-term evolution of the size distribution), Kenyon & Luu (1999), and Davis et al. (1999), and the antecedents of these papers, particularly Stern (1996) and Davis & Farinella (1997), offer results of numerical simulations of TNO size distributions. A review is given by Farinella et al. (2000).

Before comparing the numerical models with the new data in detail, we first review some of the general conclusions of these works and reexamine them in light of the new observational results, namely, the detection of a strong break to shallower distributions at $D \lesssim 100$ km, implying much lower impact rates; the stronger bounds on the bright-end α; and the clear detection of size distribution differences between two dynamical populations.

A simple analytical result of Stern (1996) is that for a population with mean eccentricity $0.03 \lesssim \langle e \rangle \lesssim 0.1$ at ≈ 42 AU, collisions are on average erosive for objects smaller than a critical diameter D^* and accretional for larger bodies. The critical diameter D^* is 100–300 km for the "strong" bodies of Durda & Stern (2000), which appear at R magnitudes 23–25.5 under the canonical albedo. Note from Figure 4 that this is the magnitude range where $\Sigma(R)$ develops a significant deficit relative to the bright-end power law. *The TNOs that are "missing" are those that are susceptible to collisional destruction.*

A general conclusion of Stern (1996) and later models is that the collision rate in the present trans-Neptunian region is too low for $D \gtrsim 200$ km objects to have been formed by pairwise accretion in 4 Gyr. The ACS results only exacerbate this difficulty, since the mass in small bodies is found to be much lower than all the models had assumed. We note, however, that the maximum size of bodies in the CKBO sample is significantly lower than that in the Excited sample, with the largest known CKBO being 60 times less massive than Pluto. These largest bodies should be largely unaffected by erosion according to all models. We can conclude that the Excited population is "older" than the CKB in the sense of cumulative number of accreting collisions. This is consistent with an origin for the Excited bodies at smaller heliocentric distances, in a denser and faster-moving section of the disk than the CKB.

Durda & Stern (2000) calculate impact and disruption rates for TNOs in the present Kuiper belt, concluding that all TNOs should be heavily cratered but that the lifetime against catastrophic destruction for $D \gtrsim 1$ km bodies exceeds the age of the solar system. We now believe the space density of $D < 100$ km bodies to be much lower than assumed in these models, perhaps by several orders of magnitude for kilometer-scale bodies. A recalculation of present-day impact rates could show that small (kilometer-scale) TNOs have negligible cratering in the past 10^9 years, and even large TNOs would have recent craters only from sub-kilometer impactors. This would argue against a collisional resurfacing effect as the source of color diversity among TNOs.

So we find the apparent paradox that objects small enough to be subject to collisional disruption are strongly depleted yet have lifetimes against disruption that are longer than the age of the solar system. A possible resolution of this paradox is that we now see the end state of the erosion process: The original CKB (and perhaps the precursor region of the Excited population) was more massive and richer in small bodies, leading to strong erosion and depletion. The erosion lowered the volume density to the point where lifetimes exceeded 10^9 yr, leaving the present "frozen" population behind. In this scenario, present-day $D \lesssim 100$ km bodies are likely all collision fragments, but they may have had little alteration in the past 3 Gyr. Surfaces would be heavily cratered but old.

At some point in the history of the CKB, the Excited population started to cross the CKB, with higher collision velocities, which would have exacerbated the erosive depletion process.

Alternatively, the accretion process in the original source disk was extremely efficient at collecting 1–10 km bodies into $D \gtrsim 100$ km bodies—but not at producing 1000 km bodies from these. A quantitative explanation for the preferred scale of accretion would be required.

4.3.4. Comparison with Detailed Models

Kenyon & Luu (1999) and Davis et al. (1999) plot the time history of the TNO size distribution in their numerical accretion/erosion models. The following seem to be generic features of the models: At the large end, the distribution becomes shallower with time as the size of the largest accreted objects increases. At the small end, the slope either approaches the Dohnanyi value (Kenyon & Luu 1999) or becomes progressively shallower (Davis et al. 1999).

The observed CKBO and Excited distributions disagree with the Kenyon & Luu (1999) models in several respects: first, the observed faint-end slope does not match the Dohnanyi value they predict; the models predict a large excess of bodies at the transition region, which is not observed; and the observed transition appears to be at the 10–100 km scale, not the kilometer scale predicted by the models. These models, however, did not attempt to model the effect of several gigayears of further collisional erosion after the formation epoch.

The agreement of the data with the Davis et al. (1999) models is fairly strong. The last time slice (1 Gyr) of their simulation shows bright- and faint-end slopes α of ≈ 0.6 and ≈ 0.0, respectively, with a transition near $D \approx 50$ km. This is remarkably similar to the observed Excited-sample magnitude distribution.

The CKBO sample resembles younger time slices in these models (~ 200 Myr) in having steeper slopes at the bright end ($\alpha_1 \approx 1.2$) and faint end ($\alpha_2 \approx 0.4$), as well as a smaller maximum object size. The transition region is at smaller diameters in the models than in the data, however. It appears in any case that the CKB is less evolved than the Excited sample in an erosion sense as well as an accretion sense. This might be expected from the smaller velocity dispersion of the present-day populations (if erosion postdates any migration of the Excited bodies) or from the higher space density or velocity of the Excited source region (if erosion predates migration).

The ACS data should serve as a target for future size evolution models. It may be particularly important for future models to consider the coupled evolution of the two (or more) cospatial dynamical populations that appear to exist currently and to have different size distributions. An interesting question is whether *any* dynamical mechanism is required to reduce the mass of the CKB to its present ≈ 0.01 $M_\oplus$ value from the ≈ 10 $M_\oplus$ levels that appear necessary to support large-object accretion, or whether erosive removal is sufficient. This question is particularly interesting in light of the absence of detected TNOs beyond 55 AU, as discussed below.

4.4. *The Source of the Jupiter-Family Comets*

It is currently widely accepted that the Jupiter-family short-period comets (JFCs) and the Centaurs are objects that have escaped from the Kuiper belt. Our *HST* ACS survey provides an estimate of the population of cometary precursors in the Kuiper belt, which we can now compare with estimates obtained from dynamical models of the Kuiper belt–JFC connection. In one of the earliest modern models of the Kuiper belt–JFC connection, Holman & Wisdom (1993) estimated that a population of 5×10^9 cometary precursors in the Kuiper belt in the 30–50 AU range is required to account for the observed population of JFCs. A more detailed calculation of essentially the same physical model by Levison & Duncan (1997) revises this estimate to 7×10^9. These calculations are based upon what can now be described as a "cold" Kuiper belt, with most objects in low-eccentricity, low-inclination orbits. In another model, Duncan & Levison (1997) postulate the "scattered disk" as a source of JFCs and estimate a population of 6×10^8 cometary precursors in the entire scattered disk, of which $\sim 1.4 \times 10^8$ are at heliocentric distances 30–50 AU. In yet another calculation, Morbidelli (1997) models the Plutinos as a source of the JFCs and estimates a required source population of 4.5×10^8 Plutino comets. A commonality of these models is the assumption that the various classes of the Kuiper belt constitute stable reservoirs of cometary precursors, and that some fraction of these objects escape into the inner solar system on gigayear timescales as a result of slow orbital chaos induced by the gravitational perturbations of the giant planets. The models differ only in the initial conditions of the Kuiper belt comets, that is, in the choice of the Kuiper belt dynamical subclass for the putative source of the JFCs.

We can convert the modeled population estimates to a surface density by assuming that the projected sky area of these estimated populations is 10^4 deg^2 (corresponding to a $\pm 15°$ latitudinal band around the ecliptic or invariable plane).

A greater challenge is to define the magnitude range of cometary precursors that correspond to the dynamical models. CLSD took this to be $R \sim 28.5$, corresponding to an object of ~ 10 km radius at heliocentric distance 40 AU, assuming the usual 4% geometric albedo. With this assumption, CLSD found agreement between their measured surface density and the required cold precursor population.

We find a surface density 3 orders of magnitude lower than the claim of CLSD. The nuclei of JFCs have now, however, been measured to have diameters predominantly in the range 1–10 km (Lamy et al. 2004). It is unfortunately unclear whether the JFC population is close to *complete* for $D \gtrsim 1$ km. It is unlikely that the JFC precursors would be smaller than the JFCs themselves, or that albedos could be significantly lower than 0.04, so we may consider $R \approx 35$ to be the faintest possible precursor population. The dynamical estimates of the surface density of trans-Neptunian cometary precursors are shown in Figure 8 by the horizontal bands in the upper right, which indicate a range of 1–10 km as the required size of the true precursors. Figure 8 also plots the 95% likelihood of the parameterized fits to observations, as described in § 3.

Extrapolation of the ACS measurements to fainter magnitudes is required to compare the TNO densities with the putative required JFC source populations. The classical belt and Plutino populations are insufficient to supply the JFCs even under the most favorable extrapolations of the ACS observations. Of course, we cannot rule out an upturn in the $\Sigma(R)$ slope at $R > 29$. A slope near $q = 3.5$ ($\alpha = 0.5$) for 1–20 km diameter Jupiter-crossing bodies is suggested by Zahnle et al. (2003) based upon crater counts on Europa and the bright terrain of Ganymede. This value is outside the allowed α_2 range for the Excited TNOs and marginal for the CKBOs. The ecliptic comet samples of Lamy et al. (2004) show a size distribution with $\alpha = 0.32 \pm 0.04$ or $\alpha = 0.38 \pm 0.06$, depending upon the inclusion of near-Earth objects with "cometary" orbits, in the range $D > 3.2$ km. Either range is marginally compatible with our Excited TNO sample, and both agree well with the measured α_2 for CKBOs. Of course, many comet nuclei are known to undergo dramatic transformation or disintegration upon entering the inner solar system, so the match with TNO sizes may be fortuitous. The apparent discrepancy between our faint-TNO size distribution and the crater sizes on the Galilean satellites requires further investigation, though it is interesting to note that both the TNO data and the crater counts have size distributions that flatten to smaller sizes.

The scattered disk remains a viable precursor population, if the precursors are near 1 km diameter and the slope at $R > 29$ is the steepest permitted for $R < 29$. Thus, with a favorable choice of precursor diameter *and* favorable extrapolation to $R \approx 34$, present scenarios for JFC origin in the scattered disk can work.

There are several factors of 2 (or more) still indeterminate in the quantitative understanding of the origin of JFCs: the completeness of the known population, the size and albedos of their precursors, the dynamical delivery rate and lifetime of the JFCs, the extent of the scattered disk, and the extrapolation to fainter magnitudes. Any definitive judgment on the origin of JFCs would clearly be premature at present.

4.5. *Constraints on the Distant Population*

The ACS survey fails to detect any object farther than 42 AU despite extending the TNO completeness limit by 2 mag from previous work. Several previous works (Allen et al. 2001; TJL;
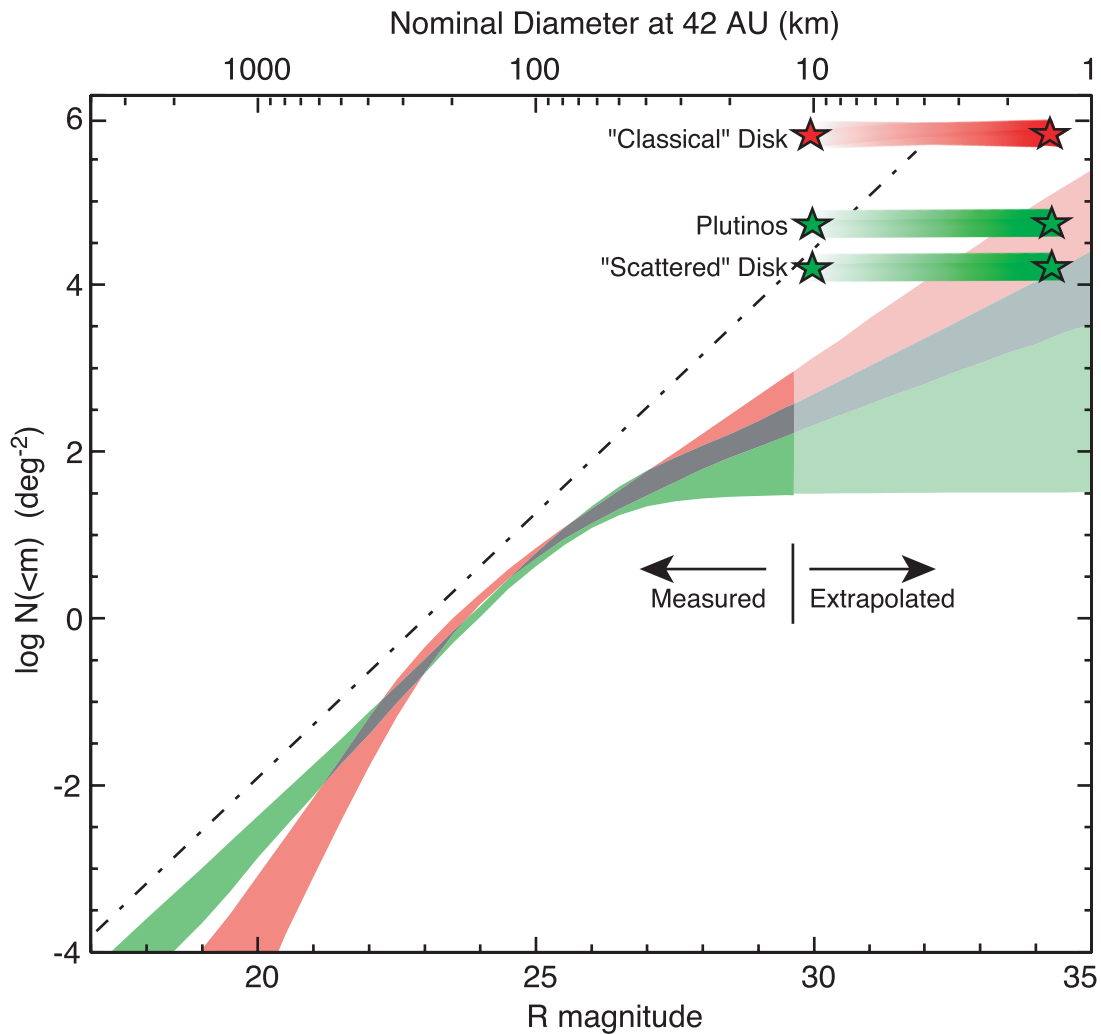
Fig. 8.—Cumulative surface density of the Excited TNO population (*green*) and of the classical Kuiper belt population (*red*), parameterized by the double power law (eq. [13]). The regions are bounded by the 95% confidence upper and lower bounds at each magnitude. The dot-dashed line is the now outdated power-law fit to the total population from TJL. The horizontal bands in the upper right are theoretical estimates based upon models of the Kuiper belt as a source of the JFCs; the assumed source population for each case is labeled. The horizontal extent is a reminder that the precursor population of known JFCs is not currently well defined, probably lying somewhere above 1 km diameter. The observed populations fall short of the surface densities calculated for putative JFC reservoirs unless a favorable extrapolation of the Excited-class density is assumed. The CKB population falls ~10 times short of the required reservoir even with favorable extrapolation.

Trujillo & Brown 2001) have shown that the space density of objects of size $D \geq 150$ km must decrease significantly beyond 50 AU from the Sun, that is, the CKB is bounded. It is possible that there is an outer belt that is deficient in objects of this size and hence undetected. We provide here a crude bound on an outer disk composed solely of smaller bodies based upon the complete absence of distant objects at $R < 28.7$ in the 0.02 deg^2 of the ACS survey.

Take a simple model in which an outer belt is localized to heliocentric distance d and contains a population of objects of diameter D. We assume that the outer belt members have albedos and material densities similar to the CKB, and that the projected mass density on the invariable plane is some multiple g times the value for the CKB derived in equation (21). For $d = 60$ AU, the magnitude limit for the ACS survey corresponds to $D \geq 37$ km (for $p = 0.04$). The invariable-plane number density of an outer disk of such objects would be $900g$ per square degree. The ACS data limit the density at 95% CL to be ≤ 150 deg^{-2}, implying $g \leq 0.17$. If D of the outer belt is larger, the limit on g is roughly unchanged, because at brighter magnitudes the area surveyed to date is

larger. The rough conclusion to be drawn is that an outer belt must either have most of its mass in objects with $D < 40$ km or must be substantially less massive than the known CKB. Caveats are that the presumed outer belt must be near the invariable plane at the ACS field, must not be more dispersed vertically than our definition of the CKB, and must not have albedo or material density dramatically different from the CKB.

This limit on the mass of an outer Kuiper belt does not apply to objects with orbits like that of Sedna, which at $d = 90$ AU is approaching its perihelion near 76 AU on a highly elliptical orbit (Brown et al. 2004). While the ACS survey would easily detect the motion of bodies anywhere on such orbits, they would be more than 500 AU distant most of the time, where even objects 1000 km in diameter would fall below our flux limit. We also do not usefully constrain the mass contained in rare large objects such as Sedna itself.

A dearth of CKB mass beyond ~50 AU may be a result of the initial conditions of solar system formation. Weidenschilling (2003) attributes a lack of CKB mass to processes from the era of planetesimal formation 4.5 Gyr ago. In his model, solid

bodies of sizes 0.1–10 m drift inward from locations of 50–100 AU because of gas drag. Interior to 50 AU, sufficient solid surface densities exist for accretion to continue. Large bodies do not accumulate outside of ~50 AU, and the exact location of the outer edge depends upon the initial disk density radial profile. This model adequately produces the observed CKBO distribution and implies that there should be little mass beyond 50 AU, even for bodies with $D < 40$ km. Alternately, the outer region of the nascent solar system could have been eliminated entirely through photoevaporation of the circumstellar disk due to UV flux from nearby OB stars (see, e.g., Throop et al. 2001). Evaporation of the disk (and entrained grains) occurs to radii as small as 50 AU in 10^5 yr in an Orion-type environment. The 10^8 or 10^9 yr CKBO formation timescale would therefore preclude formation of bodies outside the evaporation radius of perhaps 50 AU. Levison & Morbidelli (2003) suggest that the full TNO population accreted within ≈ 30 AU and was transported to its present location by interaction with a migrating Neptune; in this case we still need to explain the truncation of the original planetesimal system at 30 AU.

The lack of CKBOs beyond 50 AU may instead be a result of dynamical evolution of the outer solar system subsequent to its formation. Adams & Laughlin (2001) considered the case in which the solar system had dynamical encounters with other members of its birth cluster; these interactions could have disrupted the Kuiper belt outside of 50 AU and increased Kuiper belt object eccentricities to 0.2 or larger. Later close stellar encounters could have had similar effects: disrupting, exciting, or even removing the outer CKB (Ida et al. 2000; Larwood & Kalas 2001).

The observed data are also consistent with the interpretation that significant mass is present in the CKB outside of 50 AU and that this mass resides entirely in bodies smaller than ~40 km. It is conceivable that, within the standard model of accretion of planetesimals in a (gaseous) circumstellar disk, accretion timescales beyond 50 AU were simply too long for bodies larger than 40 km to form before the present day or some disruptive event. We note that a substantial mass in $D > 3$ km bodies in an outer Kuiper belt should be detectable by occultation surveys in the near future (Alcock et al. 2003).

A final possibility is that large bodies formed in distant orbits but have since been largely eroded or shattered to smaller sizes. It is usually difficult to destroy the largest bodies in a population, but the remaining ones could retain a sufficiently small portion of the original nebular mass that they remain undetected.

5. SUMMARY

The superior coverage and efficiency of the Advanced Camera for Surveys has allowed a survey for TNOs with $m \leq 29.2$ over 0.02 deg^2. The faint limit of the survey is determined by the criterion that a TNO have signal-to-noise ratio $\nu > 8.2$ over the 22 ks total integration time of the discovery epoch; false positive detections begin to appear below this threshold. A modest investment in present-day CPU power allows us to track, in effect, HST along each of $\approx 10^{14}$ possible TNO orbits.

Three new objects are detected, compared with the ≈ 85 that were expected from extrapolation of the power-law fit to brighter TNO survey detection rates. Artificial TNOs implanted into the data are recovered efficiently, verifying the completeness of the detection process, and the reality of the three objects is confirmed by their detection in a second set of ACS observations and the detection of the brightest one ($R \approx 27$) at the Keck Observatory.

All three detected objects are consistent with nearly circular, low-inclination orbits near $a \approx 42$ AU, although complete orbital elements will require follow-up detection (with HST).[6] Assuming an albedo of 0.04, the detected objects range from 25 to 44 km in diameter and are all well above the survey detection threshold.

No objects are detected beyond 43 AU, though we have the astrometric sensitivity to detect solar system members many hundreds of AU distant and photometric sensitivity to see 37 km objects at 60 AU. This further tightens the limits on any "outer" Kuiper belt: any outer component must be significantly less massive than the known population, or predominantly in the form of objects smaller than 40 km.

In an assemblage of data from ground-based surveys with well-quantified completeness in magnitude and invariable latitude, a crude division of the sample into "classical" and "Excited" dynamical classes reveals a difference in magnitude distribution at 96% confidence. Since the two samples have roughly similar distance distributions, we can infer a true difference in size distribution and hence in accretion/erosion history. Both populations are grossly inconsistent with a single power-law magnitude or size distribution. Double power laws give good fits to the present observations, with rolling power laws slightly less acceptable. The parametric fits indicate that the Excited population has more of its mass in large objects, so that the brightest TNOs are almost entirely in the Excited class, as has been noted before. More quantitatively, we find that under the double power laws that fit our limited sample, it is feasible to have a single body as massive as Pluto—that is, Pluto is uniquely but not anomalously large under this distribution. This is a sign that the formation of Pluto follows the same physical mechanism as the other Excited TNOs. The accretion history of the Excited bodies placed a larger fraction of the mass into the largest bodies, whereas the largest CKBO is ≈ 60 times less massive than Pluto. This is crudely consistent with scenarios in which the Excited bodies were formed at smaller heliocentric distances than the CKB (Malhotra 1993, 1995; Gomes 2003).

The total mass of the CKB (as we have defined it, with $i < 5°$) is constrained to 0.010 $M_\oplus$, with accuracy now limited solely by estimates of the albedo, distance, and material density of the bodies. This is significantly lower than previous estimates and exacerbates the difference between the present mass and the ≈ 10 $M_\oplus$ initial mass that is believed to be required to facilitate accretion of the larger TNOs. The total mass of the Excited sample is less certain because its vertical and radial extent are poorly known, but the total mass of objects within 50 AU appears similar to the CKB mass.

The detection of features in the magnitude (and, presumably, size) distribution gives fundamentally new information to be used in constraining the history of the trans-Neptunian populations, particularly the accretion and erosion history. Both dynamical samples show breaks to shallower size distributions for the $D \lesssim 100$ km population. A reevaluation of the models for collisional evolution is necessary; the assumption of collisional equilibrium with a scale-free fracturing law may need to be abandoned. Estimates of cratering and resurfacing rates in the trans-Neptunian region will also require revision. It is possible, for example, that collision rates

---

[6] Retrieval observations were conducted with HST in 2004 May.

are too low to allow significant exposure of fresh ices, a mechanism that has been invoked to explain the color diversity of TNOs (Luu & Jewitt 1996). The CKB seems to be excluded as a source of the JFCs, with the Excited class being a viable JFC reservoir only with optimistic choices for model parameters and TNO extrapolations.

The present data are consistent with a picture in which both the CKB region near 42 AU and a now vanished inner region of planetesimals were originally much more massive than at present. Accretion of 10 km bodies proceeded in both regions, advancing to 100 km bodies in the CKB; 1000 km bodies are produced in the inner region, where higher surface densities promote more rapid accretion. The migration of Neptune (or some other massive body) clears the inner region, scattering a few percent of the bodies into present "Excited" orbits. This migration or some other process also excites the eccentricities of the disk, commencing erosion among TNOs with $D < 100$ km. These smaller bodies are greatly depleted, today's population being only a fraction of the fragments produced in early collisions. Meanwhile, beyond 50 AU either there is little solid material, accretion never proceeds beyond 10 km bodies, or the modest-sized bodies are destroyed or removed by subsequent processes.

This scenario has many uncertainties and is hardly unique. Major open questions include the following: In what order and on what timescales did scattering of the Excited class, accretion of the largest bodies, and depletion of the small bodies occur? Were collisions and depletion important in the last 3 Gyr, with substantial cratering, or has the region been largely dormant? Was mass loss from the CKB purely due to erosion, or did dynamical processes eject significant mass in the form of large bodies? What is the present source reservoir for Jupiter-family comets? Why is there no "outer" Kuiper belt?

The quantitative data on TNO size and orbital distributions are improving rapidly. In the next year or two, nearly the full available sky will have been surveyed for $R \lesssim 22$ TNOs, using small telescopes (Trujillo & Brown 2003; Moody et al. 2003). Telescopes with effective aperture ≈ 4 m have surveyed hundreds of square degrees (Millis et al. 2002) and will survey thousands of square degrees (the CFHT Legacy Survey),[7] or tens of thousands (Pan-STARRS),[8] in the coming 5–10 years, to limits of $R \lesssim 24$, so a full characterization of the accretion-dominated size distribution is forthcoming. Exploring the erosion-dominated small end is of course more difficult. Eight-meter class telescopes can reach $R \approx 27$ with great effort, and recovery operations are typically more expensive than discovery until sky coverage reaches tens of square degrees. Wide-area imagers currently coming into operation on large telescopes will increase the number of known $R > 25$ TNO orbits past the current handful into the tens or hundreds in the next few years. Thousands will be possible with a Large Synoptic Survey Telescope.[9] The situation for further explorations at $R > 27$ is more bleak: the present study probably represents the limits of what can be achieved in this decade, unless *HST* is tasked to the problem for some months of time or multiconjugate adaptive optics becomes capable of providing fields of view of many arcminutes. A high-throughput space telescope imager such as *SNAP*[10] would be capable of improving on the current ACS sample by several orders of magnitude circa 2010. The most valuable information on $D \lesssim 50$ km TNOs in this decade may come from occultation surveys, for example, the nearly operational TAOS project (Alcock et al. 2003). And late next decade, the *New Horizons* spacecraft will study the composition and structure of the surfaces of Pluto and one or more TNOs, providing a cratering and chemical record.[11] It is already clear that the joint size-dynamical distribution of TNOs is rich in information to constrain the physical evolution of the outer solar system.

APPENDIX

LIKELIHOODS FOR TNO SURVEYS

Correct analyses of the TNO luminosity function $\Sigma(R)$ require a proper formulation of the likelihood of a given survey's detecting a set of objects at magnitudes $\{m_i\}$. We cover here some of the subtleties in this process that we have glossed over in § 3.2, and that have been neglected in other works as well. We then examine how well the simplified analysis described in § 3.2 approximates the likelihoods that might be obtained with full attention to the details, and we find that, for current sample sizes, these approximations do not affect the inferred bounds on the TNO populations.

A1. EXPECTED DISTRIBUTION

We presume that one is interested in constraining the differential sky density of sources $\Sigma(R)$ as a function of the magnitude R in some standard system. Because the detectability may be a function of some variability parameters V, we in fact need to know the joint distribution $\Sigma(R; V)$ and have

$$\Sigma(R) = \int dV \, \Sigma(R; V). \tag{A1}$$

We assume here that the magnitude R of interest corresponds to the time average over the light curve. The sky density will be a function of other variables, for example, dynamical quantities, but we will leave further generalization to the reader.

[7] See http://www.cfht.hawaii.edu/Science/CFHLS/.
[8] See http://pan-starrs.ifa.hawaii.edu/.
[9] See http://www.lssto.org/.
[10] See http://snap.lbl.gov/.

[11] See http://pluto.jhuapl.edu/.

The survey might not be conducted in the standard filter band, so we will denote the mean magnitude in the observed filter band as μ, so that we have

$$\Sigma_\mu(\mu; V) = \int dR\, P(\mu|R)\Sigma(R; V), \qquad (A2)$$

where we have assumed the object's variability properties to be independent of color. We assume

$$\int d\mu\, P(\mu|R) = 1. \qquad (A3)$$

A TNO may be detected by the survey, and after detection it will be assigned an observed magnitude m. The probability $P(m|\mu; V)$ of being detected *and* assigned observed magnitude m is a characteristic of the survey's methodologies, which can be determined by proper Monte Carlo tests. Note that the detection efficiency for a chosen TNO magnitude satisfies

$$0 \leq \eta(\mu; V) \equiv \int dm\, P(m|\mu; V) \leq 1 \qquad (A4)$$

because the source may not be detected at all. We can likewise integrate over V to define

$$P(\text{detection}|\mu) \equiv \eta(\mu) = \frac{\int dV\, \eta(\mu; V)\Sigma_\mu(\mu; V)}{\int dV\, \Sigma_\mu(\mu; V)} \qquad (A5)$$

or define a detection probability over R as

$$\eta(R) = \frac{\int d\mu\, dV\, \eta(\mu; V)P(\mu|R)\Sigma(R; V)}{\int dV\, \Sigma(R; V)}. \qquad (A6)$$

Note that we can determine $\eta(\mu; V)$ strictly from analysis of the survey characteristics, because μ and V fully specify the behavior of objects in the imaging. But to estimate $\eta(\mu)$ or $\eta(R)$, we also need the distributions of the TNO population over variability, color, or both, unless the detection efficiency is sufficiently independent of them.

The expected distribution of detections from a survey of solid angle Ω is

$$g(m) \equiv \frac{dN}{dm} = \Omega \int d\mu\, dV\, P(m|\mu; V) \int dR\, P(\mu|R)\Sigma(R; V). \qquad (A7)$$

Put simply, the observed distribution $g(m)$ is the convolution of the input distribution $\Sigma(R)$ with the magnitude shifts induced by color, variability, measurement error, and detection efficiency. Many real surveys are inhomogeneous, with $P(m|\mu; V)$ varying with location or time as weather conditions or integration times vary, and in these cases the expected $g(m)$ must further be convolved over these variable conditions.

A2. LIKELIHOODS

Given the function $g(m)$ derived from some $\Sigma(R, V)$, we can assign a likelihood to detection of a set $\{m_1, m_2, \ldots, m_M\}$ of detections in the survey to be

$$L(\{m_i\}|\Sigma) = dm^M \exp\left[-\int dm\, g(m)\right] \prod_{i=1}^{M} g(m_i). \qquad (A8)$$

The form of the likelihood is easily derived by considering each interval δm of magnitude to be a Poisson process with probability $\delta P = g(m)\delta m$ of having one detection and $1 - \delta P$ of zero detections.

A2.1. COMPARISON WITH GLADMAN ET AL. FORM

Gladman et al. (1998) provide an alternative form of this equation, which, in our notation and suppressing the variability parameters, is

$$L(\{m_i\}|\Sigma) = \exp\left[-\Omega \int dR\, \eta(R)\Sigma(R)\right] \prod_{i=1}^{M} \int dR\, \ell_i(R)\Sigma(R). \qquad (A9)$$

The function $\ell_i(R|m)$ "describes the uncertainty for the [true] magnitude of object i" according to Gladman et al. (1998), but the exact meaning of this is not well understood in the community. It does *not* mean a simple convolution with a Gaussian error term centered on m_i.

The identification of equation (A9) with equation (A8), up to factors of dm and Ω that are independent of the Σ-model, is clear from the following: The exponentiated quantity is in either case $\bar{N}$, the expected number of detections, given by

$$\bar{N} \equiv \int dm\, g(m)$$

$$= \Omega \int dm \int d\mu\, dV\, P(m|\mu; V) \int dR\, P(\mu|R)\Sigma(R; V) \quad (A10)$$

$$= \Omega \int dR \int dV\, dm\, d\mu\, P(m|\mu; V)P(\mu|R)\Sigma(R; V) \qquad (A11)$$

$$= \Omega \int dR\, \eta(R)\Sigma(R), \qquad (A12)$$

making use of equations (A1) and (A6).

To equate the terms under the product sign in equation (A9), we note that if the detection probability is independent of variability, we can write

$$g(m) = \Omega \int dR\, P(m|R; V)\Sigma(R), \qquad (A13)$$

so that if we identify $\ell_i(R) = P(m_i|R; V)$, then equation (A9) becomes equivalent to equation (A8). Recall that $P(m|R; V)$ is the probability of the TNO at R being *detected* at m, so its integral over m is $\eta(R) \leq 1$, and there is in any case no need to have $\int dR\, \ell_i(R) = 1$. It is hence not appropriate to take $\ell_i(R)$ to be a Gaussian about m_i with dispersion σ given by a rough magnitude uncertainty.

A simplification is possible in the case $P(m|R; V) = \eta(R)P(m - R)$, meaning that the probability of detection $\eta(R)$ is independent of the observed magnitude m for given R and the magnitude measurement error has a fixed distribution with unit normalization. This would be the case when the true magnitude is measured in follow-up observations that are distinct from the discovery observations. In this case we have

$$g(m) = \int dR\, P(m - R)[\Omega\eta(R)]\Sigma(R), \qquad (A14)$$

which implies

$$\ell_i(R) = P(m - R)\Omega_{\rm eff}(R). \qquad (A15)$$

The Gladman et al. (1998) likelihood can be misinterpreted as assuming that $\ell_i(R) = P(m_i - R)$. We see that this is incorrect— even in this simplified case it is necessary to have an additional term of $\eta(R)$ or $\Omega_{\rm eff}(R)$ under the R-integral. In many surveys, however, the detection probability is highly correlated with the observed magnitude m, so even this simple form is not applicable.

A2.2. FITTING THE AMPLITUDE

As a useful aside, consider the maximum likelihood estimate of the scale factor s that normalizes a candidate TNO distribution function of the form

$$\Sigma(R; V) = s\Sigma_0(R; V). \qquad (A16)$$

The expected distribution will clearly scale as $g(m) = sg_0(m)$, with the obvious notation. The likelihood (eq. [A8]) then has all its dependence upon s in terms

$$L \propto s^M e^{-sN_0}, \qquad (A17)$$

where N_0 is the expected number of detections $\bar{N}$ from equation (A10) for $\Sigma = \Sigma_0$. If we adopt a logarithmic prior $p(s) \propto s^{-1}$, then the Bayesian expectation values and probability distribution for s are

$$\bar{s} \equiv \langle s \rangle = M/N_0, \quad \langle N \rangle = M, \qquad (A18)$$

$$p(s > s_0) = P(M, s_0 N_0), \qquad (A19)$$

where the last right-hand side is the incomplete gamma function.[12]

If we are interested only in the shape Σ_0 of the TNO distribution, we will marginalize over the nuisance parameter s, which for the logarithmic prior yields

$$L(\{m_i\}|\Sigma_0) = \int ds\, p(s) L(\{m_i\}|\Sigma_0, s) \qquad (A20)$$

$$= N_0^{-M}\Gamma(M)\prod_i g_0(m_i) \qquad (A21)$$

$$= M^{-M}\Gamma(M)\prod_i \bar{s}g_0(m_i) \qquad (A22)$$

$$= M^{-M}\Gamma(M)e^M L(\{m_i\}|\Sigma_0, \bar{s}). \qquad (A23)$$

This analytic marginalization speeds up our likelihood analyses for the shape of Σ. Note that the formulae fail for $M = 0$, which is not surprising, since we cannot constrain the shape of Σ if we have no detections.

A3. DETECTION CUTOFF

In the following we derive some exact results for simple cases and then examine the error made in simple approximations. We will assume that in the neighborhood of the survey limit, the source density behaves as $\Sigma(R) = \Sigma_0 10^{\alpha R}$.

The simplest case to analyze is when the survey assigns a detection magnitude ρ_i to each TNO, and those brighter than a

---

[12] For $M = 0$ (no detections), the logarithmic prior leads to unnormalizable posterior distributions, and we revert to a uniform prior.

cutoff ρ_0 are accepted into the survey. From measurement noise alone, the detection magnitude usually has a Gaussian distribution about the true magnitude R with a standard deviation of $\sigma(R)$ mag. If color and variability are important, we can consider these as additional sources of scatter in the $P(\rho|R)$ distribution, as quantified in later sections; for now we consider measurement noise alone.

Consider two cases: In the first, which we will call a *snapshot* survey, the survey is halted after its detection observations, so that $m_i = \rho_i$. If we further assume that $\sigma(R)$ varies little near the completeness limit, then we have

$$g(m) = \Omega\Sigma_0 10^{\alpha m}\exp\left[\alpha^2\ln^2(10)\sigma^2/2\right]\Theta(\rho_0 - m), \quad (A24)$$

$$\bar{N} = \frac{\Omega\Sigma_0}{\alpha\ln 10}10^{\alpha\rho_0}\exp\left[\alpha^2\ln^2(10)\sigma^2/2\right], \qquad (A25)$$

$$\eta(R) = (2\pi\sigma^2)^{-1/2}\int_{-\infty}^{\rho_0} d\rho\,\exp\left[-(R-\rho)^2/2\sigma^2\right] \qquad (A26)$$

$$= \tfrac{1}{2}\,{\rm erfc}\left[(R - \rho_0)/\sqrt{2}\sigma\right]. \qquad (A27)$$

Here Θ is the step function. In this case, ignoring the difference between observed and detected magnitudes—that is, using $\Omega\Sigma(R)$ instead of $g(m)$ in the likelihood (eq. [A8]) for the $\{m_i\}$— amounts to a normalization error of $\exp\left[\alpha^2\ln^2(10)\,\sigma^2/2\right]$. The completeness follows equation (2) with $w = \sqrt{2}\sigma$.

In a second type of survey, which we will call a *magnitude follow-up* survey, the detected objects are followed up with more integration, so that the errors on magnitude are substantially reduced, and we end up with $m_i = R_i$ in the absence of color terms. Our ACS survey is well approximated in this way, since the faintest detected object has signal-to-noise ratio S/N > 20 in the full data set, and hence a magnitude uncertainty (in F606W) of less than 0.05 mag. In this case we have

$$g(m) = \Omega\Sigma(R)\eta(R), \qquad (A28)$$

where the detection efficiency $\eta(R)$ is from equation (A27) and is, in fact, independent of the form of $\Sigma(R)$. We note that in the case of a magnitude follow-up survey, the approximate likelihood in equation (8) is exactly correct.

A3.1. SIZE OF THE ERRORS

Suppose we were to conduct a snapshot survey that detects objects at $\{m_i\}$, and also a Monte Carlo survey to determine the form of $\eta(R)$, but then we get lazy in implementing equation (A8) and ignore the difference between m and R in calculating our likelihoods, using

$$g(m) = \Omega\Sigma(m)\Theta(\mu_0 - m) \qquad (A29)$$

instead of the proper form in equation (A24). Then we see that we are in effect using a luminosity function that is in error by the normalization factor $F = \exp\left[\alpha^2\ln^2(10)\sigma^2/2\right]$. We can bound this factor by noting that a TNO detection must have S/N > 6 to be reliably distinguished from noise in most detection schemes, so we expect the noise on the detected magnitude to be $\sigma < 2.5/[\ln(10)({\rm S/N})] \leq 0.18$ mag. In this case we have $F \approx 1 + 0.04(\alpha/0.7)^2$. First we note that this bias factor, if constant across all survey data, only affects the normalization of Σ and does not affect our conclusions about the shape of Σ. For $|\alpha| \leq 0.7$, the resultant 4% bias would be smaller than the Poisson errors in our analysis, which contains

only 130 total objects and is hence incapable of detecting sub-10% shifts in the presumed $\Sigma(R)$ at any magnitude.

If the bias factor F varies with R, then we might infer an incorrect shape for Σ, but again with our sample of 130 TNOs the difference is below the Poisson noise. Note that we conclude $|\alpha| \lesssim 0.7$ for all samples and magnitudes, save perhaps the bright end of the CKBO population, where we could incur a bias somewhat above 10%—but the Poisson noise is also higher in this subsample, so again the bias is negligible. Note that for surveys with significant magnitude follow-up there are no approximations in taking $g(m) = \Omega\eta(m)\Sigma(m)$, so there is no bias at all. This is the case for our ACS data, and also for the La and TB data, since we have accurate follow-up mean R magnitudes for nearly all detections.

A3.2. INHOMOGENEOUS SURVEYS

If we take this simple case literally, we would expect all surveys to report a completeness function $\eta(R)$ that follows equation (2) with $w \approx (S/N)^{-1}/\sqrt{2}$. This is true in our case, with a limiting $S/N = 8.2$ and $w = 0.08$. But most surveys report completeness functions $\eta(R)$ that are significantly broader than this form. This is generally due to inhomogeneity, as ground-based surveys must deal with varying seeing and coverage, etc., which the ACS survey does not. In effect the survey area Ω is divided into subareas Ω_k that have cutoffs ρ_k. The expected distributions $g_k(m)$ for each subsurvey may be summed to yield the total $g(m)$ for the survey. It is convenient to define the total survey area that reaches a chosen threshold:

$$\Omega_\rho(\rho) \equiv \sum_{\rho_k > \rho} \Omega_k. \qquad (A30)$$

For a *snapshot* survey, we obtain

$$g(m) = F\Omega_\rho(m)\Sigma_0 10^{\alpha m}, \qquad (A31)$$

$$\eta(R) = \frac{1}{\sqrt{2\pi\sigma^2}} \int d\rho \frac{\Omega_\rho(\rho)}{\Omega} \exp\left[-\frac{(R-\rho)^2}{2\sigma^2}\right] \qquad (A32)$$

$$= \frac{1}{2A} \int d\rho \frac{d\Omega_\rho}{d\rho} \mathrm{erfc}\left(\frac{R-\rho}{\sqrt{2}\sigma}\right). \qquad (A33)$$

The falloff in completeness $\eta(R)$ is now the convolution of the inhomogeneity with the measurement error and so will be more extended than either. But the bias F is *not* affected by the inhomogeneity, only by the measurement error, so we see that the approximation in equation (A29) can be replaced with

$$g(m) \approx \Omega_\rho(m)\Sigma(m) \qquad (A34)$$

with equal accuracy, sufficient for our purposes. For an inhomogeneous *magnitude follow-up* survey, we find that once again equation (8) is exact.

A4. COLOR ERRORS

The comparison of the observed-band magnitude μ with a density function Σ defined over a standard magnitude R can be thought of as a convolution of the expected $\Sigma(R)$ with the color distribution $P(\mu|R)$. We have assumed a single value for our F606W-R color conversion, but there is a spread in colors, which may be viewed as an additional source of stochastic uncertainty on the R magnitude of our detections. The standard deviation of $V-R$ colors is 0.10 mag (Tegler & Romanishin

2003; Tegler et al. 2003). Since F606W is nearly the union of V and R, similar to the "VR" filter used by several ground-based surveys, we estimate the scatter in F606W$-R$ to be $\sigma_{VR} \approx 0.05$ mag.

This scatter may be treated as a measurement error on R that is added in quadrature to the measurement noise. The less than 0.1 mag uncertainty due to the color conversion should have negligible effect upon the interpretation of $\Sigma(R)$, at least for the surveys under current consideration that have fewer than 100 detections and are in well-calibrated filters bounded by the V and R passbands. Note, however, that the two brightest surveys, TB and La, have very poorly defined filter bands, so the color uncertainties could be larger here. For most of these bright objects, however, a high-precision R magnitude has been found in the literature, so the color or photometry uncertainties are minimal.

A5. VARIABILITY

The variability of the TNOs can influence both the detectability and the observed magnitude m_i that is assigned to a discovery. The effect of variability upon the detection function $P(m|\mu; V)$ has not been accurately quantified for any published survey, and furthermore, the variability dependence of $\Sigma(R, V)$ is very poorly constrained, so at this point it is basically impossible to meaningfully incorporate variability into the likelihood functions.

We can nonetheless show with some basic modeling that the effect of variability upon current analyses should be minimal given the present Poisson uncertainties. The true form of $P(m|\mu; V)$ for real-life surveys is probably rather complex: most surveys require detection in two or more observation sets separated by hours to days, and the known variable TNOs have periods of 3–13 hours. We will consider some simplified forms of variability selection.

A5.1. SNAPSHOT SURVEY

A "snapshot" survey in this context observes the TNO only for a short time compared with the light-curve period, so the observed magnitude m_i is an instantaneous sample of the light curve and the detection probability is a function solely of m_i. We ignore color effects and measurement noise here, for simplicity. For the snapshot survey, let $R(t)$ be the magnitude at time t. We then have

$$P(m|R; V) = \Theta(m - \rho_0)P(m|R(t))P(R(t)|R; V), \qquad (A35)$$

where Θ is again the step function. The quantity $P(R(t)|R; V)$ is simply the distribution of instantaneous magnitudes for the chosen light curve. So $g(m)$ is the convolution of the intrinsic distribution $\Sigma(R)$ with the distributions due to variability and measurement noise. The variability in this case just acts to broaden the detection cutoff versus mean magnitude, just like a source of measurement noise.

How broad is the variability kernel? For a sinusoidal light curve with peak-to-peak amplitude A, the distribution $P(m - R) \propto [1 - (m - R)^2/4 A^2]^{-1/2}$. When a power-law $\Sigma(R)$ is convolved with this distribution, the resultant $\Sigma_m \equiv dN/dm$ is enhanced by the factor

$$F = 1 + (A\alpha \ln 10)^2/16 + (A\alpha \ln 10)^4/1024 + \cdots. \qquad (A36)$$

Even in the worst case of a square-wave light curve, the bias factor is $F = \cosh[A\alpha \ln(10)/2]$, which is ≈ 2 times larger.

Our 2003 BF$_{91}$, along with 2001 QG$_{298}$, is the most highly variable of the $\approx$60 TNOs tested for variability to date, with $A \approx 1.1$ mag (Trilling & Bernstein 2004; Sheppard & Jewitt 2004). With this A and $\alpha \leq 0.7$, the surface density for instantaneous magnitudes is $F \leq 1.20$ higher than the $\Sigma(R)$ for mean magnitudes.

One might expect small (faint) TNOs to be less symmetric and hence more variable than bright TNOs, though this is not yet borne out. But it can never be the case that they have uniformly high amplitudes A, because pole-on rotators must have zero amplitude. The formulae of Lacerda & Luu (2003) for the light-curve amplitudes of triaxial ellipsoids in minimum-energy rotation can be used to show that a population of identically shaped TNOs with randomly oriented rotation axes will have a roughly uniform distribution of light-curve amplitudes between 0 and A_{max}. We might expect a similar result for variability due to surface features rather than gross body shape. In this case the population-averaged enhancement factor will be

$$F \approx 1 + (A_{max}\alpha \ln 10)^2/48. \qquad (A37)$$

Take, as a pessimistic case, a population of TNOs that are all sufficiently asymmetric to have light-curve amplitudes as large as 2003 BF$_{91}$ if viewed $90°$ from the rotation pole. Then we find the difference between the instantaneous and mean magnitude distributions to be $F \leq 1.07$, less than 7%. Thus the error made by failing to distinguish these cases is below the Poisson noise of the current samples.

A5.2. WORST-CASE MODELS

The worst possible bias in the TNO sample due to variability would be if the selection were based upon peak (or minimum) flux over the light curve. A simplistic scenario that might spawn such a selection effect is for a survey that consists of many repeated observations of each target, in which a "detection" consists of the TNO rising above the threshold in *one or more* of the epochs. Once detected, the TNO is found in all epochs, and we report a mean magnitude. In this scenario, the reported magnitude is an unbiased estimator of the true R, but the detection criterion is a step function of the peak flux over the light curve, $\eta(R, V) = \Theta(\rho_c - (R - A/2))$, for a light curve with peak-to-peak amplitude A. Note that in this case, as for the snapshot model in the previous paragraph, there is a bias *toward* detection of highly variable TNOs. Hence, increased variability in the faint population would tend to *steepen* the derived $\Sigma(R)$, as opposed to the flattening we detect in the ACS sample.

Conversely imagine that the detection criterion is that the TNO be above threshold in *all* of the epochs. In this case $\eta(R, V)$ will be a function solely of the *minimum* flux over the light curve, and the detection is biased *against* high variability at a given mean R.

Again take a pessimistic view that A is uniformly distributed between 0 and $A_{max} \approx 1$ mag. Then (in the absence of noise) the selection function $\eta(R)$ drops linearly from unity at $\rho_0 - A/2$ to zero at ρ_0. This closely resembles the error function form in equation (2) with $m_{50} = \rho_0 - A_{max}/4$ and $w = A_{max}/8$. Hence, in this worst-case scenario the effect of variability is to shift our completeness limit brightward by $\leq$0.3 mag and broaden the cutoff by $\leq$0.15 mag.

A6. IS A SIMPLE TREATMENT SUFFICIENT?

In analyzing the surveys taken to date, we have taken a simplified form for the likelihood, embodied by equation (8). We have seen that this form is exact in the case of a magnitude follow-up survey with a fully realistic Monte Carlo derivation of $\Omega_{eff}(R) = \Omega\mu(R)$ that is properly marginalized over the variability and color of the TNOs. Technically, the simplified likelihood is incorrect for our analysis for the following reasons:

1. The middle-magnitude surveys have no follow-up and are "snapshot" surveys, meaning that $g(m)$ from equation (A31) is more appropriate. We have shown that the F-factor is smaller than Poisson errors, and the difference between $\Omega_\rho(m)$ and $\eta(m)$ is only a convolution by the relatively sharp function equation (A27) from magnitude errors of $\sigma \lesssim 0.2$ mag. If we avoid the regions where $\eta < 0.2$, then the effect on the likelihood is small.

2. The Monte Carlo estimates of $\eta(R)$ in most surveys ignore errors in color terms. The effect is to broaden $\eta(R)$ by $\lesssim$0.05 mag in quadrature.

3. The Monte Carlo estimates of completion ignore variability. For short-exposure surveys, this is equivalent to a sub-7% mismeasure of the underlying $\Sigma(R)$. In the worst imaginable case of selection effects, it could lead to a shift in the completeness limit by $\leq$0.3 mag and a broadening of $\leq$0.15 mag.

4. For technical reasons, the Monte Carlo for the ACS data yields $\Omega_\rho(m)$ rather than the slightly broader $\eta(R)$ function.

5. Some readers may not trust the completeness tests or magnitude error estimates of our or other surveys.

To test the effect of these approximations on our results, we have reanalyzed the survey data after artificially broadening the $\eta(R)$ cutoff width w by 0.3 mag for the ACS and TB surveys. We also shift the cutoff m_{50} of the ACS completion function brightward by 0.3 mag to test the import of a substantial misestimate of our completeness or variability treatments.

Note that we do not apply these completeness changes to all the surveys, just those at the ends of the magnitude ranges, because we are more interested in errors that might have influenced the shape of the $\Sigma(R)$ fits. We find that no combination of these tweaks to the assumed $\eta(R)$ functions causes a significant shift in the (α_1, α_2)-contours of Figure 6 or in any of the quantities calculated herein. When we shift m_{50} of the ACS survey brightward, the ability to discriminate α_2 for the two classes is weakened (distinct α_2 values are still strongly suggested), and the extrapolation to the JFC source population can be higher. Our main conclusions, however, remain valid: a break in the power-law $\Sigma(m)$ is required, there is a significant deficit of small bodies, and the CKB and Excited classes have distinct size distributions, with the latter having clearly shallower α_1. We therefore conclude that a simplified treatment of the likelihoods is currently adequate. Simply put, the ACS survey has only three detections, so there is no need to be too careful with subtle variability or color effects.

When uniform TNO surveys with $\gg$100 detections are available, however, a more careful treatment will be required. In particular, careful attention to the effect of variability may be needed, and the likelihood analyses should perform the proper integrals to obtain $g(m)$ in the case that accurate follow-up magnitudes are not available, because the distinction between the discovered magnitude m and the true magnitude R is important at the few-percent level.

REFERENCES

Adams, F. C., & Laughlin, G. 2001, Icarus, 150, 151
Alcock, C., et al. 2003, Earth Moon Planets, 92, 459
Allen, R. L., Bernstein, G. M., & Malhotra, R. 2001, ApJ, 549, L241
———. 2002, AJ, 124, 2949
Anderson, J. 2003, in The 2002 *HST* Calibration Workshop, ed. S. Arribas, A. Koekemoer, & B. Whitmore (Baltimore: STScI), 13
Beckwith, S. V. W., Henning, T., & Nakagawa, Y. 2000, in Protostars and Planets IV, ed. V. Mannings, A. P. Boss, & S. S. Russell (Tucson: Univ. Arizona Press), 533
Bernstein, G. M., Allen, R. L., & Trilling, D. E. 2004a, in preparation
Bernstein, G. M., & Khushalani, B. 2000, AJ, 120, 3323
Bernstein, G. M., Zacharias, N., & Smith, J. A. 2004b, in preparation
Bertin, E., & Arnouts, S. 1996, A&AS, 117, 393
Brown, M. E., Kulkarni, S. R., & Liggett, T. J. 1997, ApJ, 490, L119
Brown, M. E., & Pan, M. 2004, AJ, 127, 2418
Brown, M. E., & Trujillo, C. A. 2004, AJ, 127, 2413
Brown, M. E., Trujillo, C., & Rabinowitz, D. 2004, ApJL, submitted (astro-ph/0404456)
Buratti, B. J., et al. 2003, Icarus, 162, 171
Chiang, E. I., & Brown, M. E. 1999, AJ, 118, 1411
Chiang, E. I., & Jordan, A. B. 2002, AJ, 124, 3430
Cochran, A. L., Levison, H. F., Stern, S. A., & Duncan, M. J. 1995, ApJ, 455, 342 (CLSD)
Davis, D. R., & Farinella, P. 1997, Icarus, 125, 50
Davis, D. R., Farinella, P., & Weidenschilling, S. J. 1999, in Lunar and Planetary Science XXX (Houston: Lunar Planet. Inst.), No. 1883
Dohnanyi, J. W. 1969, J. Geophys. Res., 74, 2531
Duncan, M. J., & Levison, H. F. 1997, Science, 276, 1670
Durda, D. D., & Stern, S. A. 2000, Icarus, 145, 220
Farinella, P., Davis, D. R., & Stern, S. A. 2000, in Protostars and Planets IV, ed. V. Mannings, A. P. Boss, & S. S. Russell (Tucson: Univ. Arizona Press), 1255
Gladman, B., Kavelaars, J. J., Nicholson, P. D., Loredo, T. J., & Burns, J. A. 1998, AJ, 116, 2042
Gladman, B., Kavelaars, J. J., Petit, J.-M., Morbidelli, A., Holman, M. J., & Loredo, T. 2001, AJ, 122, 1051
Gomes, R. S. 2003, Icarus, 161, 404
Greaves, J. S., et al. 1998, ApJ, 506, L133
Hahn, J. M., & Malhotra, R. 1999, AJ, 117, 3041
Holman, M. J., & Wisdom, J. 1993, AJ, 105, 1987
Ida, S., Larwood, J., & Burkert, A. 2000, ApJ, 528, 351
Kant, I. 1755, Allgemeine Naturgeschichte und Theorie des Himmels (Königsberg: J. F. Petersen)
Kenyon, S. J., & Luu, J. X. 1999, ApJ, 526, 465
Kenyon, S. J., & Windhorst, R. A. 2001, ApJ, 547, L69

Koerner, D. W., Sargent, A. I., & Ostroff, N. A. 2001, ApJ, 560, L181
Kuchner, M. J., & Holman, M. J. 2003, ApJ, 588, 1110
Lacerda, P., & Luu, J. 2003, Icarus, 161, 174
Lamy, P. L., Toth, I., Fernández, Y. R., & Weaver, H. A. 2004, in Comets II, ed. M. C. Festou, H. U. Keller, & H. A. Weaver (Tucson: Univ. Arizona Press), in press
Larsen, J. A., et al. 2001, AJ, 121, 562
Larwood, J. D., & Kalas, P. G. 2001, MNRAS, 323, 402
Levison, H. F., & Duncan, M. J. 1997, Icarus, 127, 13
Levison, H. F., & Morbidelli, A. 2003, Nature, 426, 419
Levison, H. F., & Stern, S. A. 2001, AJ, 121, 1730
Luu, J., & Jewitt, D. 1996, AJ, 112, 2310
Malhotra, R. 1993, Nature, 365, 819
———. 1995, AJ, 110, 420
———. 1996, AJ, 111, 504
Marcy, G. W., Cochran, W. D., & Mayor, M. 2000, in Protostars and Planets IV, ed. V. Mannings, A. P. Boss, & S. S. Russell (Tucson: Univ. Arizona Press), 1285
Millis, R. L., Buie, M. W., Wasserman, L. H., Elliot, J. L., Kern, S. D., & Wagner, R. M. 2002, AJ, 123, 2083
Moody, R., Schmidt, B., Alcock, C., Goldader, J., Axelrod, T., Cook, K. H., & Marshall, S. 2003, Earth Moon Planets, 92, 125
Morbidelli, A. 1997, Icarus, 127, 1
O'Dell, C. R., & Beckwith, V. W. 1997, Science, 276, 1355
Pan, M., & Sari, R. 2004, Icarus, submitted (astro-ph/0402138)
Press, W. H., Teukolsky, S. A., Vetterling, W. T., & Flannery, B. P. 2002, Numerical Recipes in C++ (2nd ed.; Cambridge: Cambridge Univ. Press)
Sheppard, S. S., & Jewitt, D. 2004, AJ, 127, 3023
Smith, B. A., & Terrile, R. J. 1984, Science, 226, 1421
Stern, S. A. 1996, AJ, 112, 1203
Tegler, S. C., & Romanishin, W. 2003, Icarus, 161, 181
Tegler, S. C. Romanishin, W., & Consolmagno, G. J. 2003, ApJ, 599, L49
Throop, H. B., Bally, J., Esposito, L. W., & McCaughrean, M. J. 2001, Science, 292, 1686
Trilling, D. E., & Bernstein, G. M. 2004, AJ, submitted
Trujillo, C. A., & Brown, M. E. 2001, ApJ, 554, L95
———. 2003, Earth Moon Planets, 92, 99
Trujillo, C. A., Jewitt, D. C., & Luu, J. X. 2001, AJ, 122, 457 (TJL)
Tyson, J. A., Guhathakurta, P., Bernstein, G., & Hut, P. 1992, BAAS, 24, 1127
Weidenschilling, S. J. 2003, in Lunar and Planetary Science XXXIV (Houston: Lunar Planet. Inst.), No. 1707
Weissman, P. R., & Levison, H. F. 1997, in Pluto and Charon, ed. S. A. Stern & D. J. Tholen (Tucson: Univ. Arizona Press), 559
Zahnle, K., Schenk, P., Levison, H., & Dones, L. 2003, Icarus, 163, 263